

Chapter 2. Analysis of Archimedean Spiral Antenna

The Archimedean spiral antenna is a popular of frequency independent antenna. Previous wideband array designs with variable element sizes (WAVES) have used the Archimedean spiral antenna as the radiating element. The Archimedean spiral is typically backed by a lossy cavity to achieve frequency bandwidths of 9:1 or greater. In this chapter the Numerical Electromagnetics Code (NEC) was used to simulate the Archimedean spiral. Also, several Archimedean spirals were built and tested to validate the results of the NEC simulations. Since the behavior of an Archimedean spiral antenna is well known, the simulation and measurement results presented in this chapter serve to validate the results found for the star spiral in Chapter 4 and the array simulations in Chapters 5 and 6.

2.1 Theory

A self-complementary Archimedean spiral antenna is shown in Fig. 2.1. A spiral antenna is self-complementary if the metal and air regions of the antenna are equal. The input impedance of a self-complementary antenna can be found using Babinet's principle, giving

$$Z_{metal} Z_{air} = \frac{\eta^2}{4} \quad (2.1)$$

where η is the characteristic impedance of the medium surrounding the antenna. For a self-complementary Archimedean spiral antenna in free space the input impedance should be

$$Z_{in} = \frac{\eta_o}{2} = 188.5\Omega \quad (2.2)$$

Each arm of an Archimedean spiral is linearly proportional to the angle, ϕ , and is described by the following relationships

$$r = r_o\phi + r_1 \text{ and } r = r_o(\phi - \pi) + r_1 \quad (2.3)$$

where r_1 is the inner radius of the spiral. The proportionality constant is determined from the width of each arm, w , and the spacing between each turn, s , which for a self-complementary spiral is given by

$$r_o = \frac{s + w}{\pi} = \frac{2w}{\pi} \quad (2.4)$$

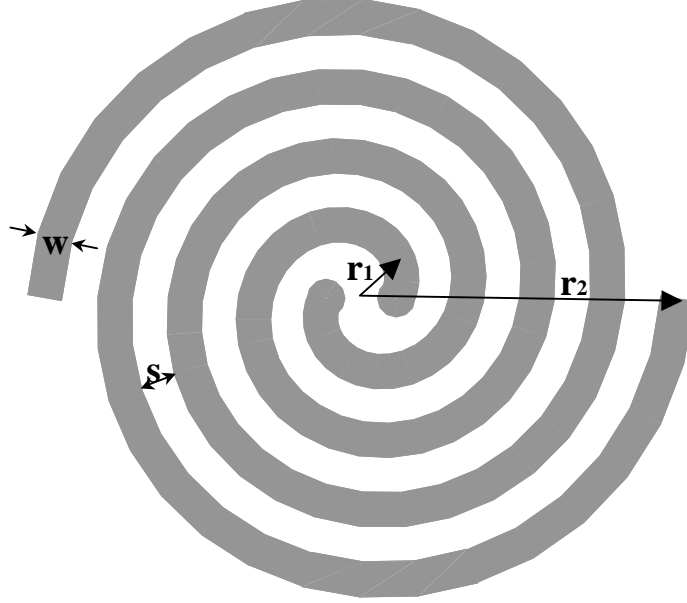


Figure 2.1 Geometry of Archimedean spiral antenna.

The strip width of each arm can be found from the following equation

$$s = \frac{r_2 - r_1}{2N} - w = w \quad (2.5)$$

assuming a self-complementary structure. Thus the spacing or width may be written as

$$s = w = \frac{r_2 - r_1}{4N} \quad (2.6)$$

where r_2 is the outer radius of the spiral and N is the number of turns. The above equations apply to a two-arm Archimedean spiral, but in some cases four-arm spirals may be desired. In this case the arm width becomes

$$w_{4-arm} = \frac{r_2 - r_1}{8N} \quad (2.7)$$

and the proportionality constant is

$$r_{o,4-arm} = \frac{4w}{\pi} \quad (2.8)$$

The Archimedean spiral antenna radiates from a region where the circumference of the spiral equals one wavelength. This is called the active region of the spiral. Each arm of the spiral is fed 180° out of phase, so when the circumference of the spiral is one wavelength the currents at complementary or opposite points on each arm of the spiral add in phase in the far field. The low frequency operating point of the spiral is determined theoretically by the outer radius and is given by

$$f_{low} = \frac{c}{2\pi r_2} \quad (2.9)$$

where c is the speed of light. Similarly the high frequency operating point is based on the inner radius giving

$$f_{high} = \frac{c}{2\pi r_1} \quad (2.10)$$

In practice the low frequency point will be greater than predicted by (2.9) due to reflections from the end of the spiral. The reflections can be minimized by using resistive loading at the end of each arm or by adding conductivity loss to some part of the outer turn of each arm. Also, the high frequency limit may be less than found from (2.10) due to feed region effects.

2.2 Simulation

The Numerical Electromagnetics Code 4 (NEC4) was used as the primary simulation tool in this dissertation (Burke, 1992). IE3D and measurements were used in some cases to validate the results found with NEC4. However, due to problem size and computer run-time constraints, NEC4 is a more practical code for this application. There are two main areas of concern with modeling an Archimedean spiral in NEC4. The first concern is the appropriate model for the feed region and the second is the relationship between wire diameter and strip width to be used in the model. Another potential problem area is modeling a lossy cavity. This can be done by using a lossy ground plane in NEC4, but most simulations will be done in free space to avoid this problem since it is not significant to the work presented in this dissertation.

For the Archimedean spiral in free space a single feed wire connects each arm to a single voltage source at the center of the feed wire. Typically a wire radius of one quarter the desired strip width is used in simulations as an appropriate transformation from strip width to wire diameter. That is

$$a = \frac{w}{4} \quad (2.11)$$

where a is the wire radius and w is the width of each spiral arm. So, a single feed wire and the relationship of (2.11) will be used as starting points in the simulations. Another important parameter in setting up the NEC4 simulation is the value of the inner radius, r_1 . Through trial and error it was found that frequency independent behavior was achieved only when the inner radius was equal to the strip width or spacing between turns, $r_1 = w = s$. Solving (2.6) for the inner radius equal to the width gives

$$r_1 = \frac{r_2}{4N + 1} \quad (2.12)$$

To demonstrate the effect of the inner radius on the problem, consider an Archimedean spiral antenna with an outer radius of $r_2 = 0.1m$ and 8 turns. The inner radius will be varied from half the radius found using (2.12) to three times the radius found using (2.12). The spiral is positioned in free space and a single feed wire and source are used as previously described. The spiral parameters are summarized in Table 2.1, and Fig. 2.1 shows a picture of the corresponding spirals with different inner radii. The effect of changing the inner radius is to increase or decrease the size of the hole in the center of the spiral and the size of the feed wire. Fig 2.3 shows the input impedance of the spirals as the inner radius is varied. When the inner radius is less than the arm width the real part of the input impedance is less than the desired 188 ohms, and when the inner radius is greater than the arm width the real part of the input impedance is greater than expected. Also, when the inner radius is not equal to the arm width, both the real and imaginary parts of the input impedance vary greatly with frequency. For a frequency-independent, self-complementary spiral the input impedance should be 188 ohms and flat over a wide frequency range. This behavior is best achieved in NEC4 when the inner radius is equal to the arm width, $r_1 = w$.

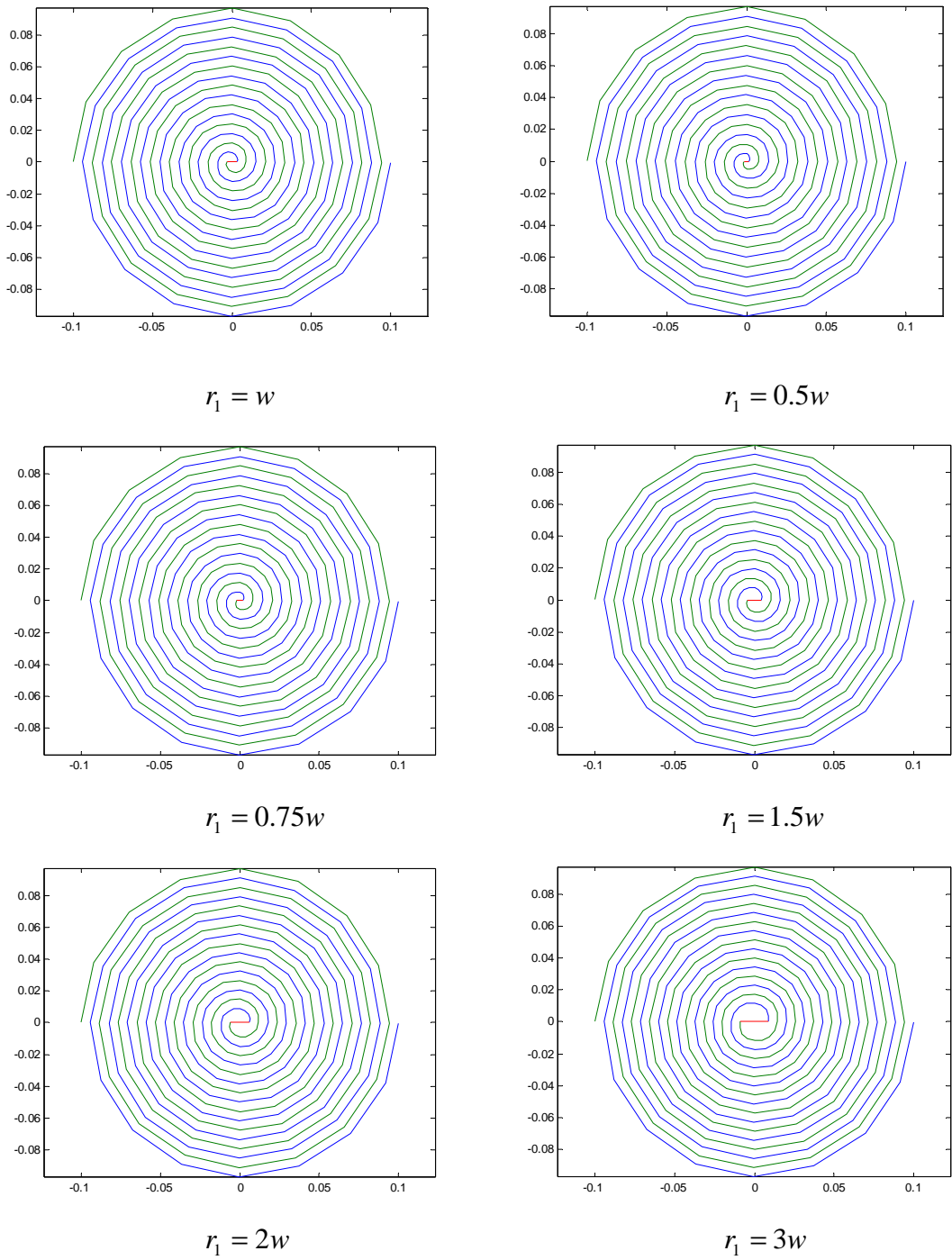


Figure 2.2 Geometry of Archimedean spirals with various values of the inner radius.

Table 2.1 Parameters for Archimedean spiral with various inner radii. For all cases there are 16 segments per turn and 5 segments on the feed wire.

Parameter	$r_1 = w$	$r_1 = 0.5w$	$r_1 = 0.75w$	$r_1 = 1.5w$	$r_1 = 2w$	$r_1 = 3w$
r_2 , [cm]	10	10	10	10	10	10
N	8	8	8	8	8	8
r_1 , [cm]	0.3	0.15	0.23	0.45	0.61	0.91
w , [cm]	0.3	0.31	0.31	0.3	0.29	0.28
a , [cm]	0.0757	0.0769	0.0763	0.0746	0.0734	0.071

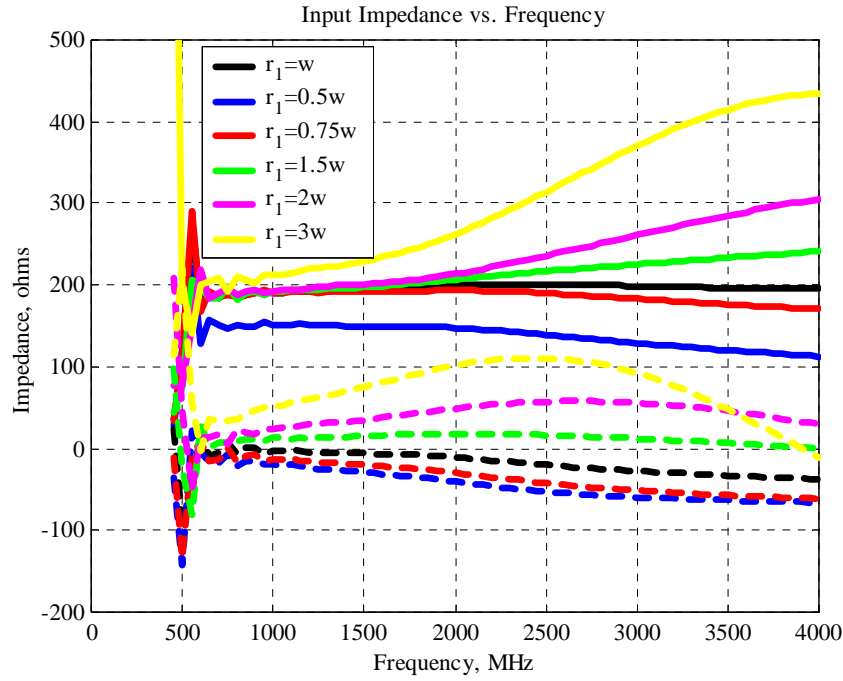


Figure 2.3 Simulated input impedance versus frequency for various values of the inner radius. The solid lines represent the real part of the input impedance and the dashed lines represent the imaginary part of the input impedance.

It is also necessary to validate the relationship between wire radius and wire width given in (2.11). Consider the same spiral from the example above: $r_1 = 0.3\text{cm}$, $r_2 = 10\text{cm}$, 8 turns, and the radius found using (2.11) is $a_o = 0.0757\text{cm}$. The effect of varying the wire radius is shown in Fig. 2.4. When the radius is smaller than a_o the real

part of the input impedance is significantly higher than expected but the imaginary part of the input impedance is improved. For a larger radius, the real part of the input impedance is smaller than 188 ohms and less flat with frequency. The imaginary part of the input impedance is also worse. Fig 2.4 shows that the typical relationship between wire radius and wire width, $a = w/4$, is a good approximation for simulating a spiral antenna in NEC4.

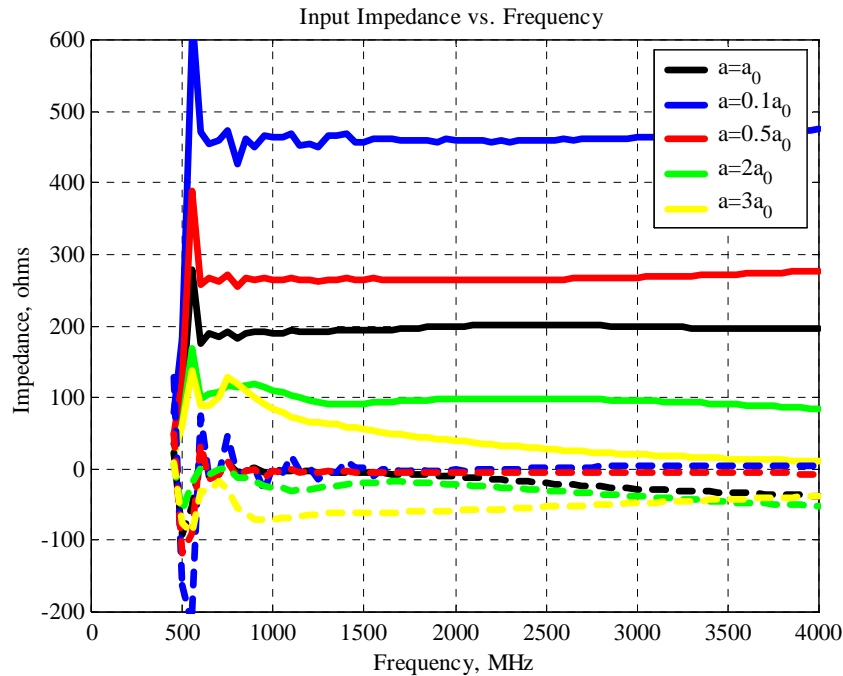


Figure 2.4 Simulated input impedance versus frequency for various values of wire radius. The solid lines represent the real part of the input impedance and the dashed lines represent the imaginary part of the input impedance.

Now that the appropriate NEC model for the Archimedean spiral has been determined, the antenna performance can be evaluated. The voltage standing wave ratio (VSWR) is typically used to measure antenna bandwidth. The VSWR for the spiral modeled above, $r_1 = 0.3cm$, $r_2 = 10cm$, 8 turns, $a = 0.0757cm$, 16 segments per turn, and 5 segments on the feed wire, is shown in Fig. 2.5. The VSWR referenced to 188Ω is less than 2:1 for frequencies greater than 530 MHz. The input impedance and VSWR are more sensitive to the small changes in geometry discussed above compared to the radiation patterns and axial ratio. However, the radiation patterns and axial ratio must

also be verified in NEC4 since they will be important later in the array analysis. Fig. 2.6 shows the total far-field patterns for the same spiral modeled above: $r_1 = 0.3cm$, $r_2 = 10cm$, 8 turns, $a = 0.0757cm$, 16 segments per turn, and 5 segments on the feed wire. The maximum gain at each frequency point, assuming no impedance mismatch, is plotted in Fig. 2.7. The general trend is for the gain to increase with frequency as expected.

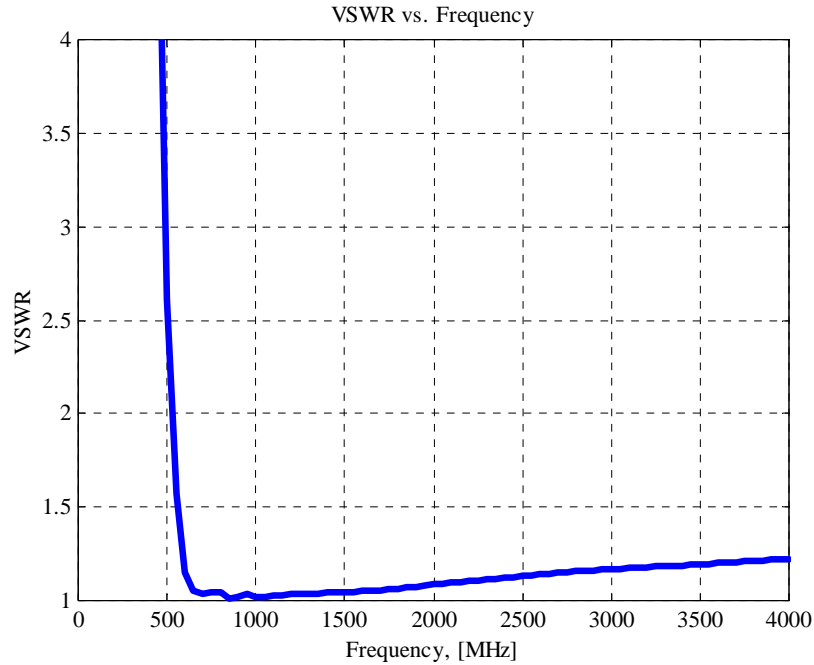


Figure 2.5 Simulated VSWR versus frequency.

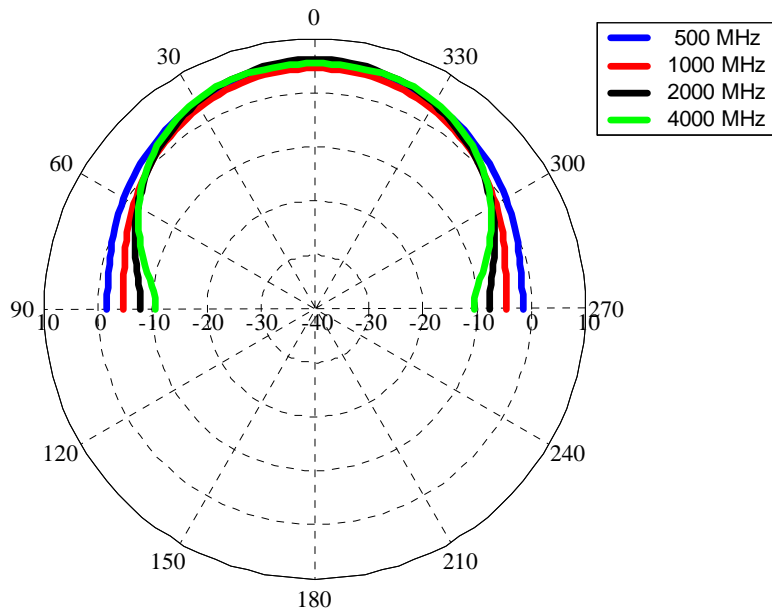


Figure 2.6 Simulated radiation pattern plots versus theta for $\phi = 0^\circ$.

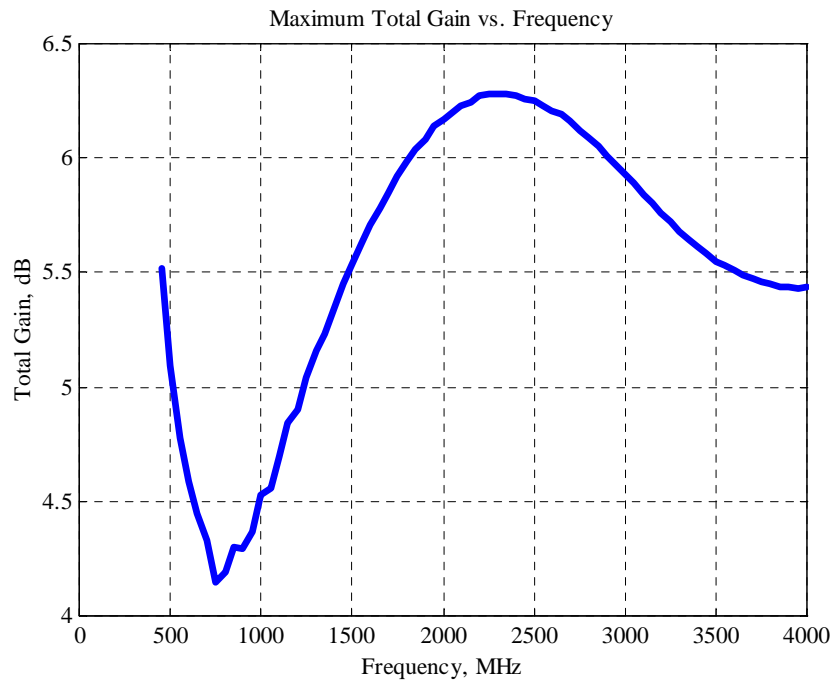


Figure 2.7 Simulated maximum gain versus frequency for $\phi = 0^\circ$.

The axial ratio is also a very important parameter for spiral antennas. It is desired that the Archimedean spiral have circular polarization broadside to the antenna. The simulated boresight ($\theta = 0^\circ$) axial ratio versus frequency is shown in Fig. 2.8. Perfect circular polarization is equal to an axial ratio of 0 dB, but an axial ratio less than 3 dB is often considered acceptable. The axial ratio is less than 3 dB for frequencies of approximately 700 MHz and higher compared to a VSWR less than 2:1 for frequencies of about 530 MHz and greater. The difference in these two performance criteria can be attributed to reflections from the end of each arm. The reflected wave has opposite sense polarization compared to the outward traveling wave and has significant impact on the axial ratio at the lower frequencies. Both the low frequency axial ratio and VSWR can be improved by resistive loading at the end of each arm of the spiral. The axial ratio versus theta is also of interest. Fig. 2.9 shows the axial ratio of the example spiral versus theta for various frequencies. It is desirable for the axial ratio to be less than 3dB over the broadest range of theta angles possible. The spiral has a 3dB or less axial ratio for $-60^\circ < \theta < 60^\circ$ and frequencies above 1000 MHz. Also, as seen in Fig. 2.8, the spiral has very poor axial ratio performance at 500 MHz.

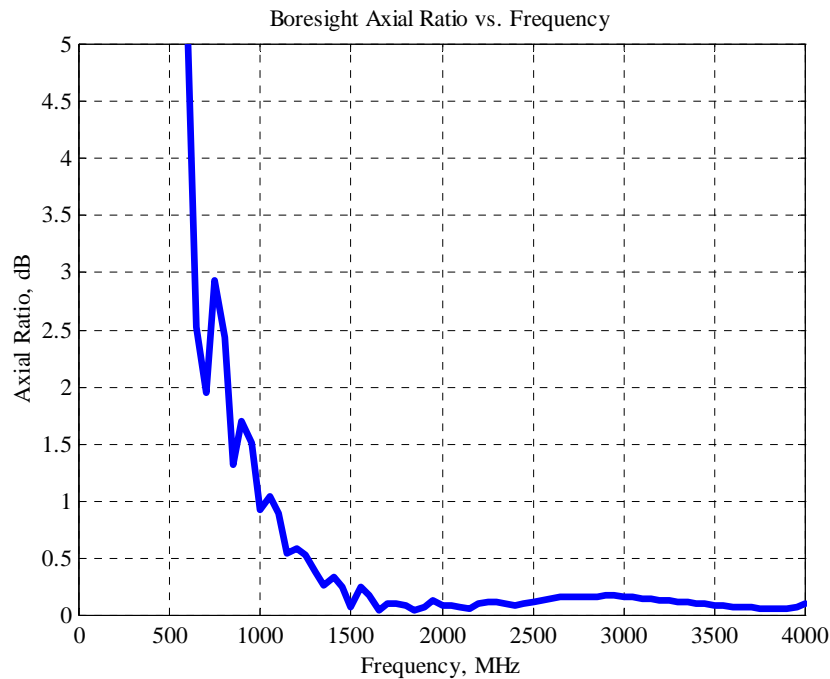


Figure 2.8 Simulated boresight axial ratio versus frequency for $\phi = 0^\circ$.

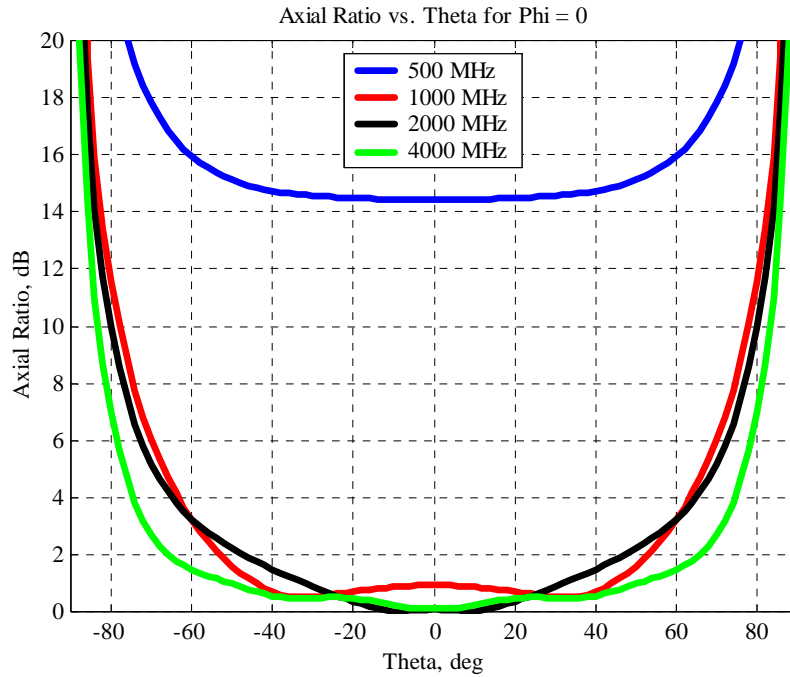


Figure 2.9 Simulated axial ratio versus theta for various frequencies, $\phi = 0^\circ$.

The convergence criteria and limitations of NEC4 must also be investigated. In the previous examples 16 segments per turn and 5 segments on the feed wire were used. Fig. 2.10 shows the VSWR of the example spiral used above for different combinations of number of segments per turn and segments on the feed wire. The VSWR is referenced to 188 ohms. Fig. 2.10 is not intended to demonstrate a rigorous convergence test. As in the earlier study of inner radius dimension and the strip width to wire diameter ratio, the objective here is to find the combination of segments per turn and feed segments that yield the best results compared to the 188Ω input impedance predicted by theory. The figure clearly shows that both the number of segments per turn and the number of segments on the feed wire affect the results. The best results are found with 10 segments per turn and 3 segments on the feed wire and the second best convergence is found with 16 segments per turn and 5 segments on the feed wire. As frequency is increased there is a general trend for the cases with more segments to degrade faster. This is probably due to the breakdown in the thin wire approximation used by NEC4. For most cases in this dissertation 16 segments per turn and 5 segments on the feed wire will be used for

consistency since simulations of the star spiral require 16 segments per turn to generate the correct geometry. From Fig 2.10 it can be seen that for 16 segments per turn and 5 segments on the feed the VSWR is less than 2:1 for frequencies less than about 11 GHz, which is much higher than necessary for the array simulations found in later chapters of this thesis.

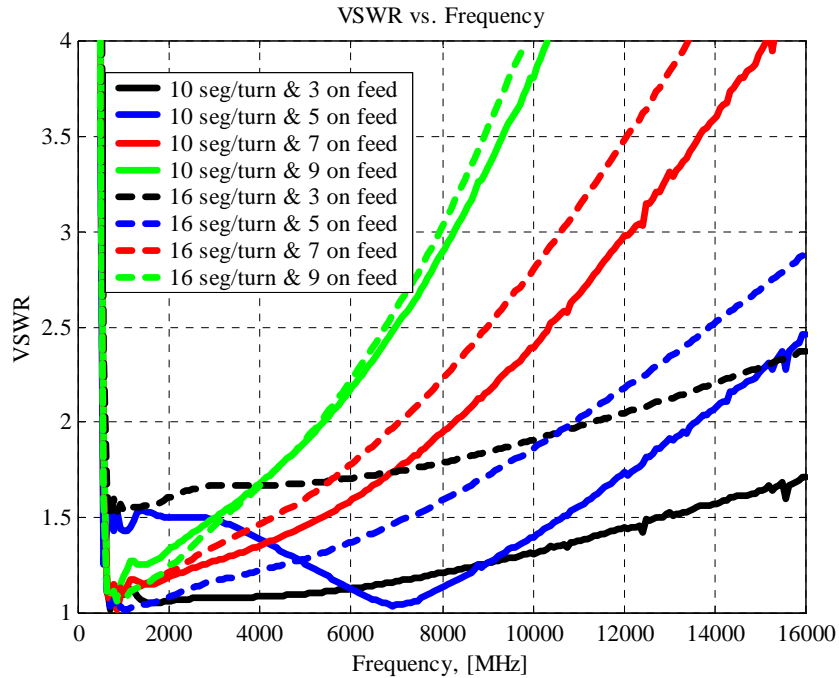


Figure 2.10 Performance test for Archimedean spiral with various numbers of segments per turn and segments on the feed wire.

The performance test presented in Fig. 2.10 shows that satisfactory results are found using 16 segments per turn, but a more rigorous convergence test is needed to validate the results. A standard convergence test is shown in Fig. 2.11. The figure shows the real part of the input impedance of the spiral versus number of segments per turn for a few different frequencies. Five segments are used on the feed wire for all cases. Fig. 2.11 shows that 16 segments per turn is adequate for numerical convergence since the input resistance is fairly flat above 16 segments per turn. The breakdown of the thin wire approximation used in NEC4 is also clearly shown in Fig. 2.10. For frequencies above 8000 MHz the input impedance begins to deviate from the expected value of 188Ω as the

segment length becomes too large compared to the wavelength. For example, for 16 segments per turn, the longest segment is approximately 1.5 times the wavelength at 12000 MHz. At 16000 MHz the theoretical high frequency cutoff for the spiral is just exceeded which further explains poor results.

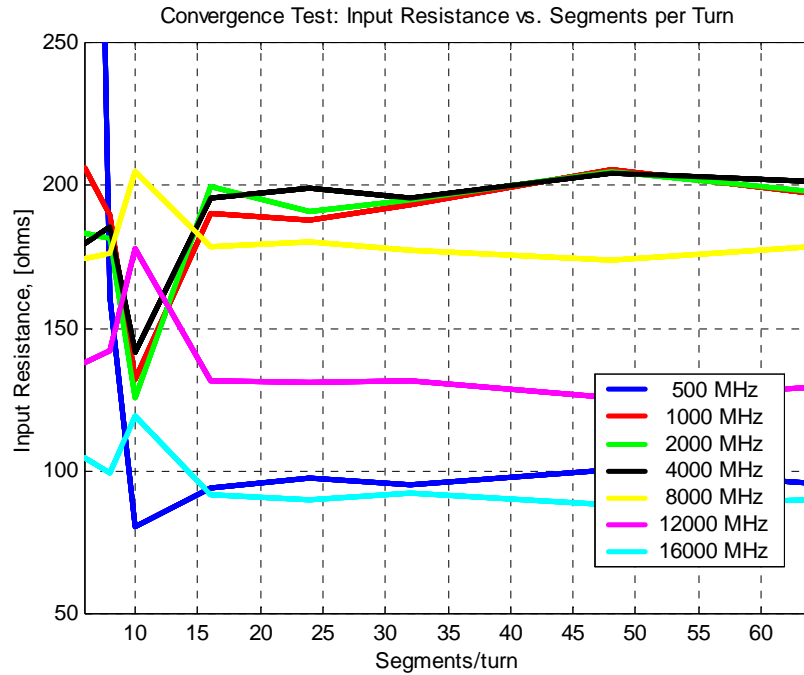


Figure 2.11 Convergence plot of input resistance versus number of segments per turn.

2.3 Addition of Loss and Resistive Loading

The addition of conductivity loss or resistive loading to the end of each spiral arm can be used to reduce reflections from the end of each arm. The question is how much loss or resistance should be added and what best represents a practical antenna. In NEC4, a resistive load can be added to any segment or conductivity can be assigned to any segment. Both techniques reduce reflections from the end of the arm and improve the low frequency VSWR and axial ratio.

Consider the example Archimedean spiral simulated in the previous section: $r_1 = 0.3cm$, $r_2 = 10cm$, 8 turns, $a = 0.0757cm$, 16 segments per turn, and 5 segments on the feed wire. A resistive load of 188 ohms has been added to the last segment, last 2 segments, and last 3 segments of each arm. The 188 ohms was chosen to match the desired input impedance of a self-complementary Archimedean spiral. A comparison of

the VSWR for the spiral with and without resistive loading is shown in Fig. 2.12. The theoretical low frequency cutoff with this spiral is 477 MHz, which corresponds to the red curve with 2 loads per arm. It is not practical to add excessive loss so that the antenna operates below its theoretical limit. The addition of resistive loss improves the impedance bandwidth of the spiral at the expense of the antenna gain. Fig. 2.13 shows a plot of the maximum gain versus frequency for a number of load cases. At 500 MHz there is about a 2 dB loss in gain when 2 loads per arm are used. Another important parameter affected by the addition of loss is the axial ratio plotted in Fig. 2.14. This plot shows a continuous improvement in the low frequency axial ratio as the number of loads is increased. The plots show that the addition of loss to the end of each arm only effects the low frequency performance of the antenna, but the amount of loss must be determined by the tradeoffs between improved VSWR, axial ratio, and reduced gain.

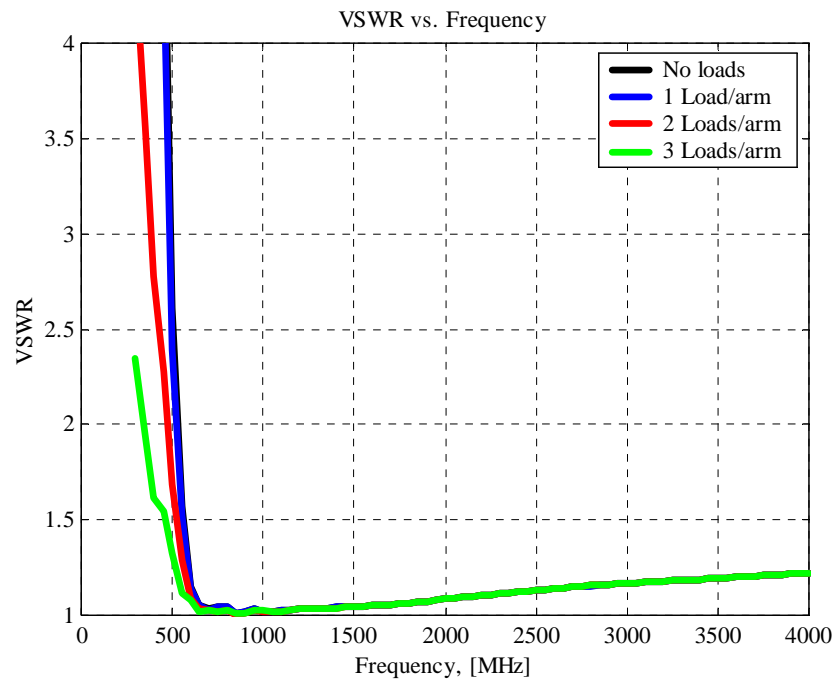


Figure 2.12 VSWR versus frequency for different number of loads. The loads are added to the outer segments of each arm of the spiral. Each load is 188 ohms.

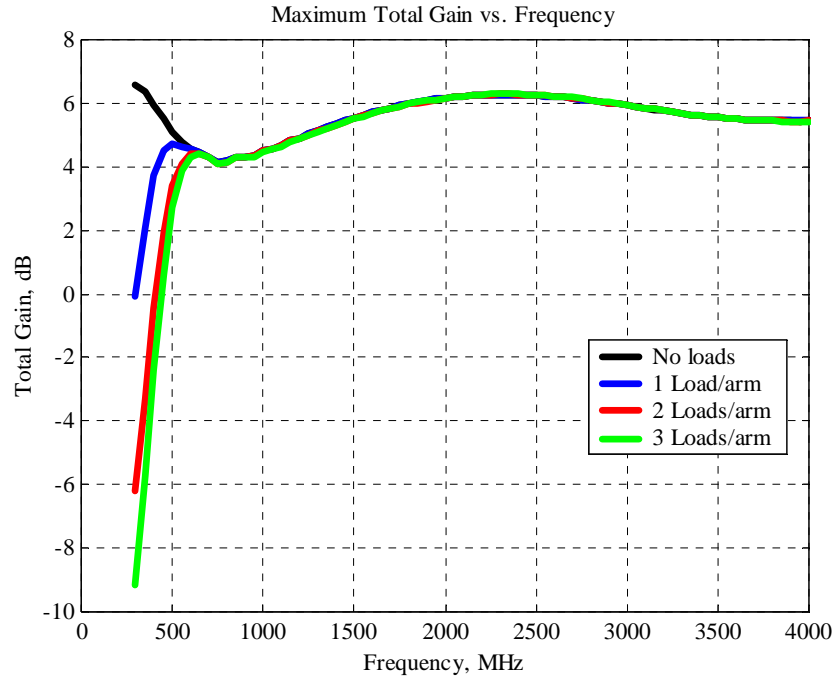


Figure 2.13 Maximum gain versus frequency for different number of loads. The loads are added to the outer segments of each arm of the spiral. Each load is 188 ohms.

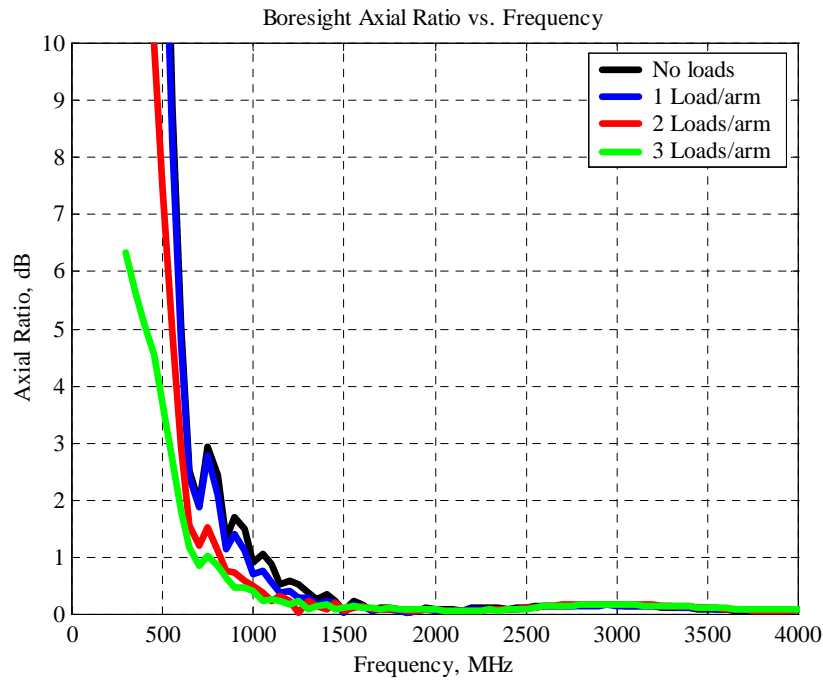


Figure 2.14 Axial ratio versus frequency for different number of loads. The loads are added to the outer segments of each arm of the spiral. Each load is 188 ohms.

Loss may also be added by introducing a finite conductivity to a segment. Figures 2.15, 2.16, and 2.17 show the VSWR, maximum gain, and axial ratio for the example spiral when finite conductivity is used. The conductivity is added to the last half turn of each arm of the spiral. The results for using resistive loads versus finite conductivity are very similar, but the conductivity method allows for slightly better control. Since both methods correspond to practical techniques for adding loss to a spiral, the best method may depend on the particular application.

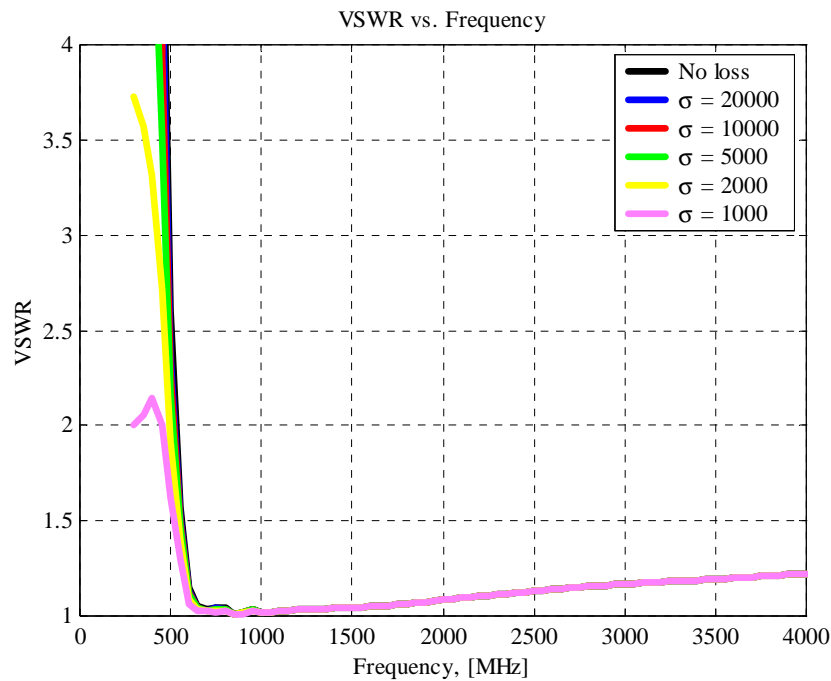


Figure 2.15 VSWR versus frequency for different conductivities. The conductivity is added to the last half turn of each arm of the spiral.

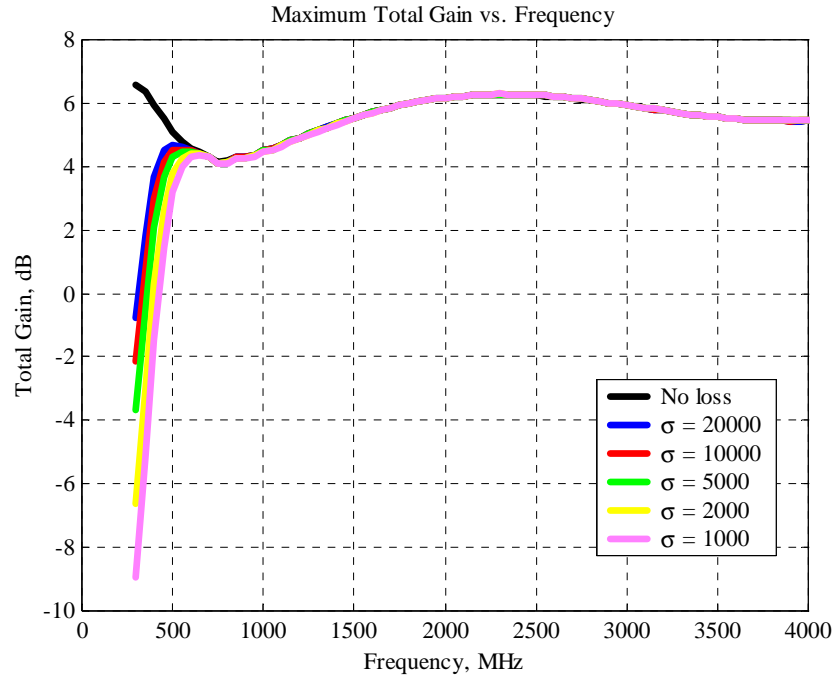


Figure 2.16 Maximum gain versus frequency for different conductivities. The conductivity is added to the last half turn of each arm of the spiral.

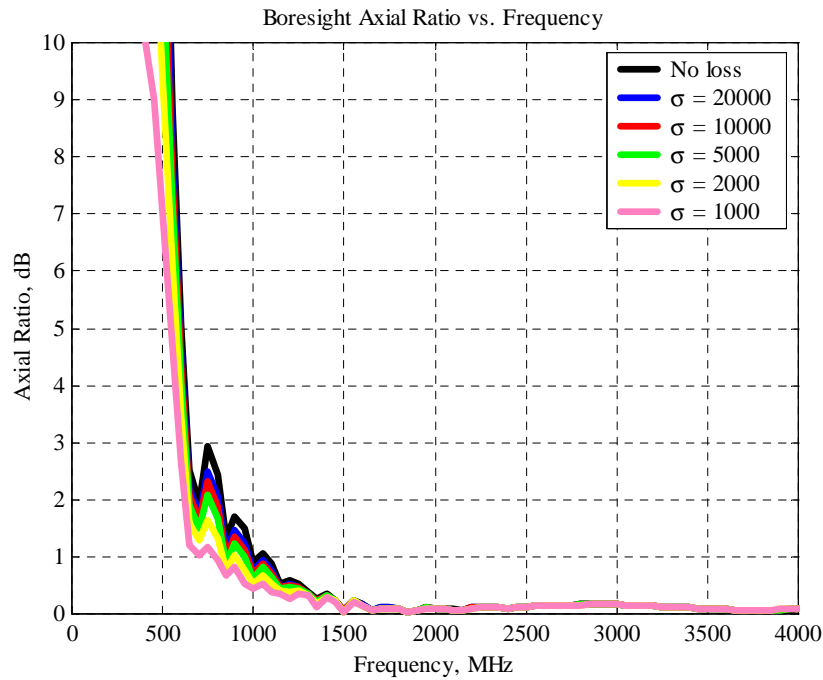


Figure 2.17 Axial ratio versus frequency for different conductivities. The conductivity is added to the last half turn of each arm of the spiral.

2.4 Ground Plane Effects

Spiral antennas are typically backed by a lossy cavity, which restricts the radiation to one hemisphere and improves impedance bandwidth at the expense of a 2-3 dB gain reduction due to the decrease in antenna efficiency. Recently the use of spiral antennas with conducting ground planes has become more popular. These types of spirals have more gain but the axial ratio and pattern bandwidths are drastically reduced compared to spirals backed by lossy cavities. Most of the spiral element and array simulations in this thesis will be simulated in free space, but for some cases it may be desirable to use a ground plane.

There are two approaches that can be used to add a ground plane and still obtain three or more octaves of bandwidth. The first is to use a lossy ground plane. This option allows the specification of a relative permittivity and conductivity of the ground plane to be used in a reflection coefficient approximation or a Sommerfeld/Norton approximation to the ground plane. The other possibility is to construct a conical shaped ground plane that maintains quarter wavelength spacing between the spiral and the ground plane in the vicinity of the active region of the spiral (Drewniak, et al., 1986).

The spiral that has been used throughout this chapter has $r_1 = 0.3cm$, $r_2 = 10cm$, 8 turns, $a = 0.0757cm$, 16 segments per turn, and 5 segments on the feed wire. For this spiral, Fig. 2.18 shows the effect on the VSWR of a ground plane using the reflection coefficient approximation with various levels of loss. The spiral is spaced a quarter wavelength, $d = 0.0375m$, above the ground plane for a center frequency of 2000 MHz. The VSWR is greatly affected by the ground plane below 2000 MHz. However, even for the perfect electric conductor (pec) ground case, the VSWR is essentially unaffected above 2000 MHz. A lossy ground plane with a relative permeability of $\mu_r = 1$ and a conductivity of $\sigma = 0.005$ yields results equivalent to those found in free space. The axial ratio shows very similar trends to the VSWR as seen in Fig. 2.19. The radiation pattern bandwidth is also very important. For a pec ground, a null is expected at 4000 MHz for the spacing, $d = 0.0375m$, used in this example, which corresponds to $\lambda/2$ spacing above ground. The radiation patterns versus theta plots are shown in Fig. 2.20 at

a frequency of 4000 MHz. Once again the results show that values of $\mu_r = 13$ and $\mu_r = 7$ give satisfactory results, but a $\mu_r = 1$ agrees best with the free space results.

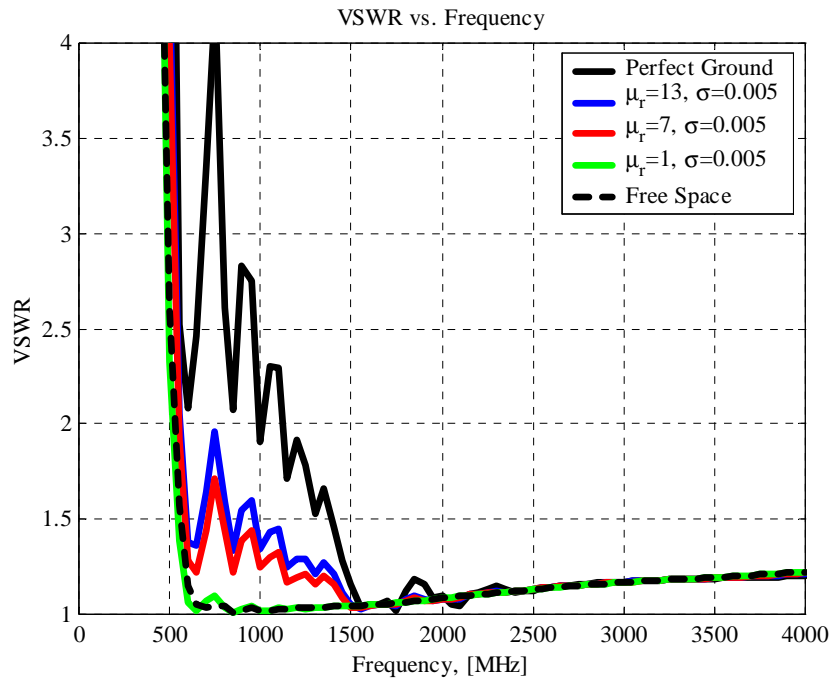


Figure 2.18 VSWR versus frequency for different levels of ground plane loss.

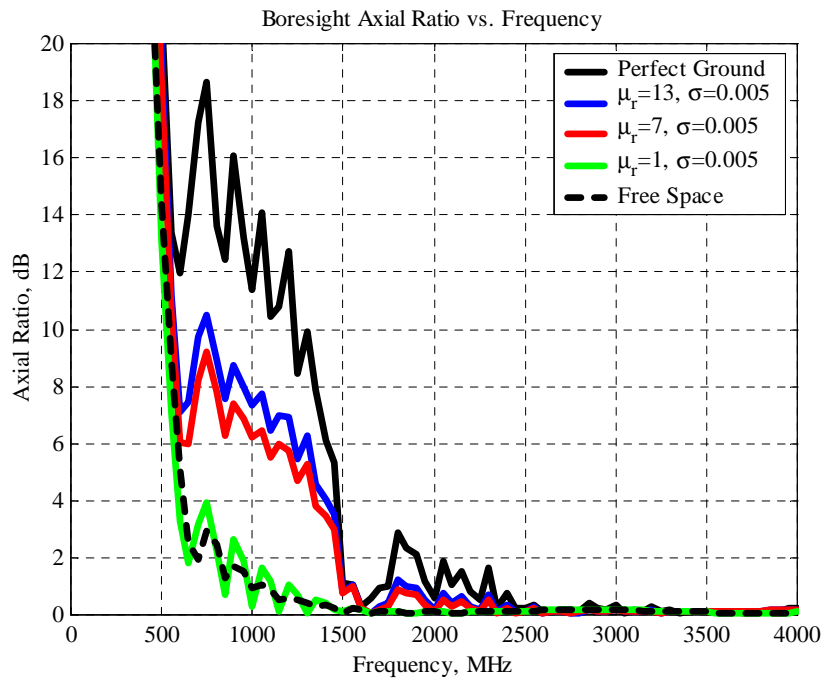


Figure 2.19 Axial Ratio versus frequency for different levels of ground plane loss.

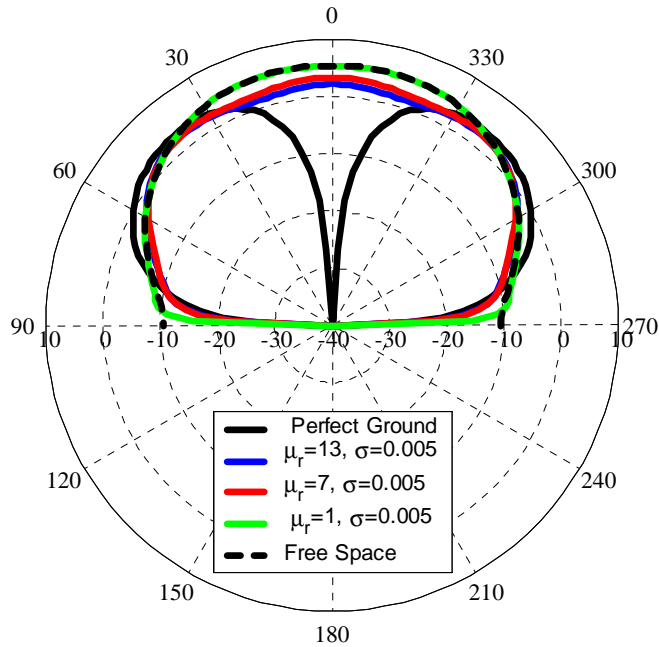


Figure 2.20 Radiation pattern plots versus theta for different levels of ground plane loss. $\phi = 0^\circ$, $f = 4000$ MHz.

The use of a conical ground plane is a technique for achieving wideband behavior without adding loss (Drewniak, et al., 1986). For instance, the example spiral has a outer radius of $r_2 = 10\text{cm}$ corresponding to an approximate low frequency cutoff of 500 MHz and the inner radius of $r_1 = 0.3\text{cm}$ corresponds to an approximate high frequency cutoff of 15 GHz. These two frequencies along with the outer radius of the spiral are used to determine the dimensions of the conical ground plane, as shown in Fig. 2.21. The conical ground plane was simulated using a wire grid model with 13 radials and 11 rings, placed on a planar, perfectly pec ground plane. The spiral is placed at a height of $d = 0.095\text{m}$ above the ground plane, which corresponds to quarter wavelength spacing at a frequency of 789 MHz. The tip of the conical ground plane is 0.005m below the center of the spiral, which corresponds to quarter wavelength spacing at a frequency of 15 GHz.

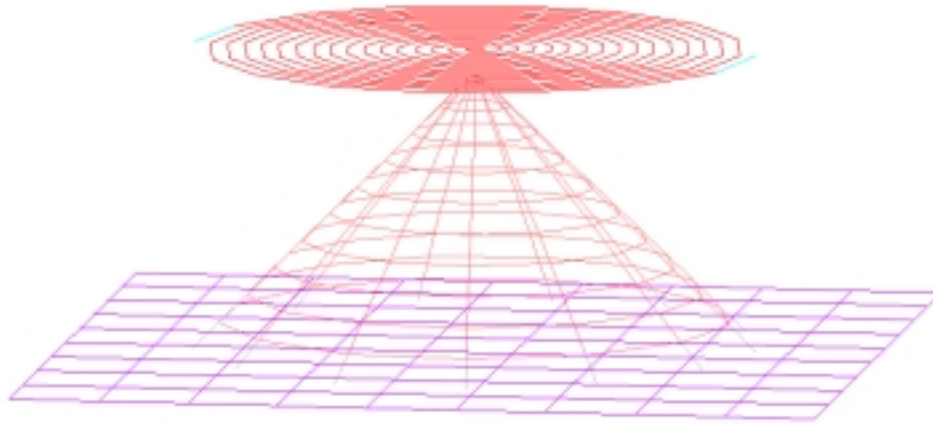


Figure 2.21 Geometry of spiral antenna with conical ground plane.

A comparison of the performance of the conical ground plane versus other types of ground planes is shown in the Figs. 2.22-2.26. Fig. 2.22 shows the VSWR for the various types of ground simulations and for free space. For a 2:1 VSWR, the conical ground performs equally as well as free space or the lossy ground and out performs the perfect ground by about 1000 MHz at the low frequency. The broadside gain of the spiral antenna using different types of ground planes is presented in Fig. 2.23. The gain of the spiral using a perfect ground plane shows the formation of a null around 4000 MHz as expected from the pattern plots of Fig. 2.20. The gain using a conical ground fluctuates from 2.5 dB to 12 dB, but the points of low gain do not indicate null formation. Figure 2.24 shows the patterns for a frequency range covering three octaves. The patterns are all well formed with a small amount of ripple seen at certain frequencies. Patterns for the points of minimum gain are shown in Fig. 2.25. Once again the patterns show some ripple and they are not as uniform as in free space but they do not have nulls. The final parameter of interest is axial ratio, shown in Fig. 2.26. The conical ground plane slightly out performs the perfect ground plane in terms of maximum axial ratio in the frequency band of interest, but for an axial ratio less than 3 dB they perform about the same.

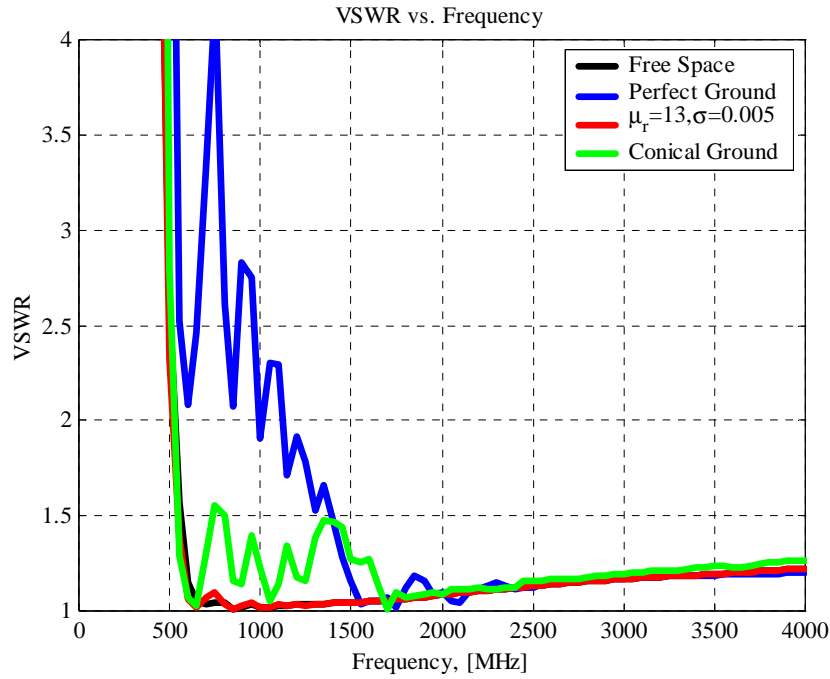


Figure 2.22 Comparison of VSWR versus frequency for different types of ground planes.

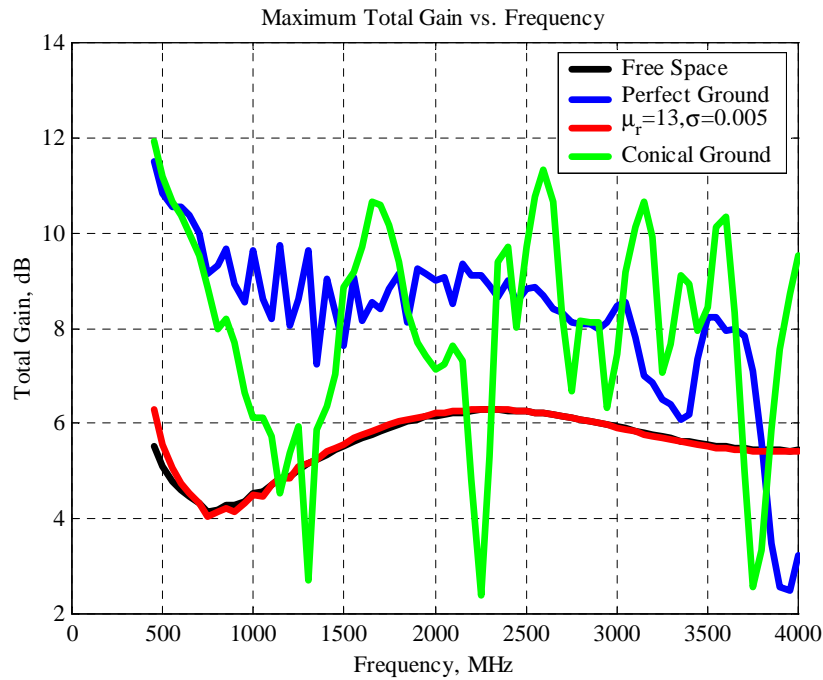


Figure 2.23 Comparison of gain versus frequency for different types of ground planes.

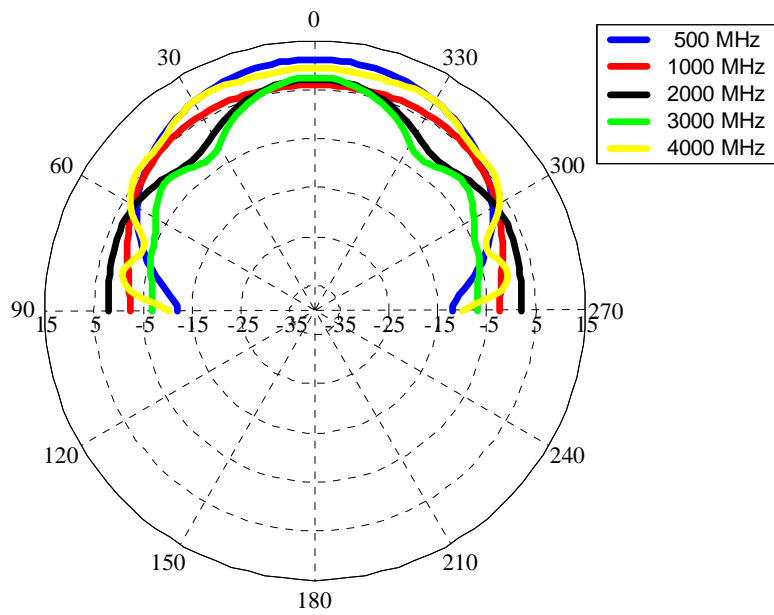


Figure 2.24 Radiation pattern plots versus theta for various frequencies covering three octaves of frequency bandwidth. $\phi = 0^\circ$

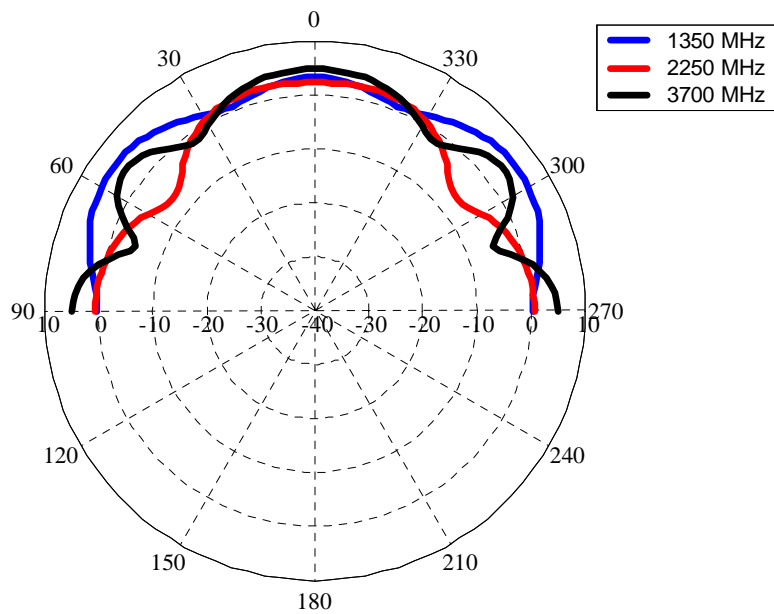


Figure 2.25 Radiation pattern plots versus theta for frequencies at the minimum gain points. $\phi = 0^\circ$

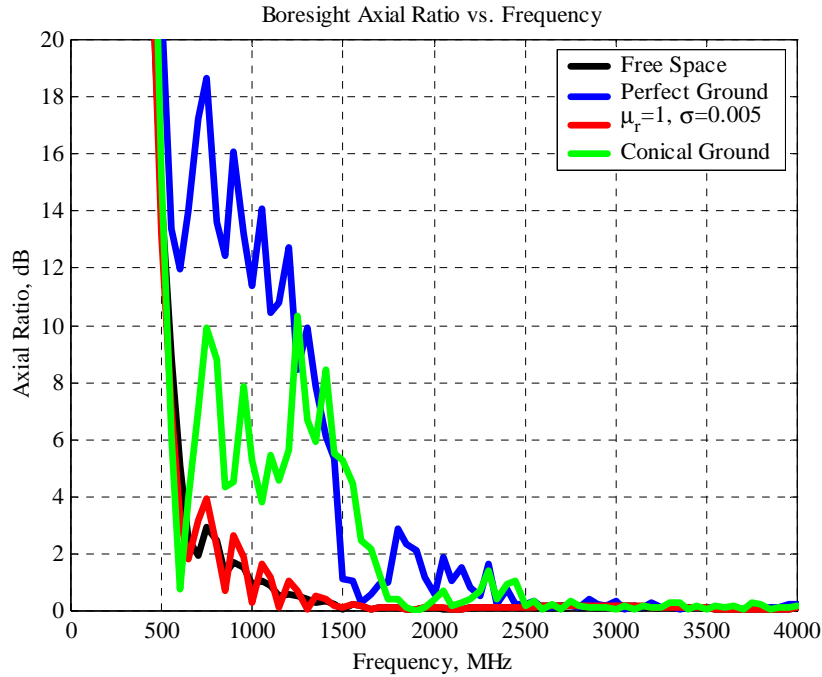


Figure 2.26 Comparison of axial ratio versus frequency for different types of ground planes.

The results for the conical ground plane presented above could be extended, however, some general trends have been observed. First, placing the spiral closer (than used in this example) to a perfect electrically conducting ground beneath the conical structure can reduce the ripple observed in the radiation patterns at the expense of a greater VSWR at the low end of the frequency range. An optimum spacing should exist to maximum the both parameters. Secondly, the points of minimum gain seen in Fig. 2.20 vary as the structure of the conical ground plane is changed. It may be possible to shift the minimum gain points out of the frequency bands of interest by appropriately picking the number of radials and rings used to model the conical ground plane. Also, the use of a solid conical ground plane may eliminate this problem entirely.

2.5 Measurements

A number of circular spirals were built and measured to validate the theoretical and simulated results. The spirals were printed on Rogers RT/duroid 5880, which has a dielectric constant of 2.2. The pattern measurements were performed in the Virginia Tech anechoic chamber using a near-field scanner, and a HP 8753 vector network

analyzer was used to measure input impedance. The input impedance of the spirals was measured using a 2-port measurement technique developed by Davis (1995). The input impedance is found from the 2-port s-parameters using the following equation

$$Z_{in} = 2Z_o \frac{1 + s_{11} - s_{12}}{1 - s_{11} + s_{12}} \quad (2.13)$$

where $Z_o = 50\Omega$.

For ease of comparison to the star spiral in Chapter 4, each circular spiral that was built and tested had an outer radius of $r_2 = 0.0507m$ and $N = 16$ turns. Fig. 2.27 shows the measured input impedance for three circular spirals with different strip widths compared to a simulated spiral. The simulated result and spiral #1 have the standard width of $w = 4a = w_o$, which gives the best results for a complementary spiral as detailed in Section 2.2. Spiral #2 has a strip width based on the average of the free space and dielectric relative permittivities, $w = 2w_o / (1 + \sqrt{2.2}) = 0.81w_o$. Lastly, spiral #3 has a strip width based on an earlier attempt to match the simulated results to the measured results. The resulting strip width is $w = w_o / 1.15\sqrt{2.2} = 0.59w_o$. The three spirals are shown in Fig. 2.28. The strip width increases from left to right.

The curves of Fig. 2.27 show the same trends as seen in Fig. 2.4, where the effect of different wire radii was investigated. Spiral #2, $w = 0.81w_o$, is closest to a complementary spiral and compares best to the simulated spiral, particularly at lower frequencies. Spiral #1, $w = w_o$, has a strip width greater than that of a complementary spiral due to the effect of the dielectric, and as expected from Fig. 2.4 the input resistance is less than 188 ohms. Spiral #3 has a strip width thinner than that of a complementary spiral which results in an input resistance greater than 188 ohms. All of the measured results show a fair amount of noise and the input resistance tends towards 100 ohms with increasing frequency. The noise can be reduced by performing the measurements in an anechoic chamber, as was done here, but not completely eliminated.

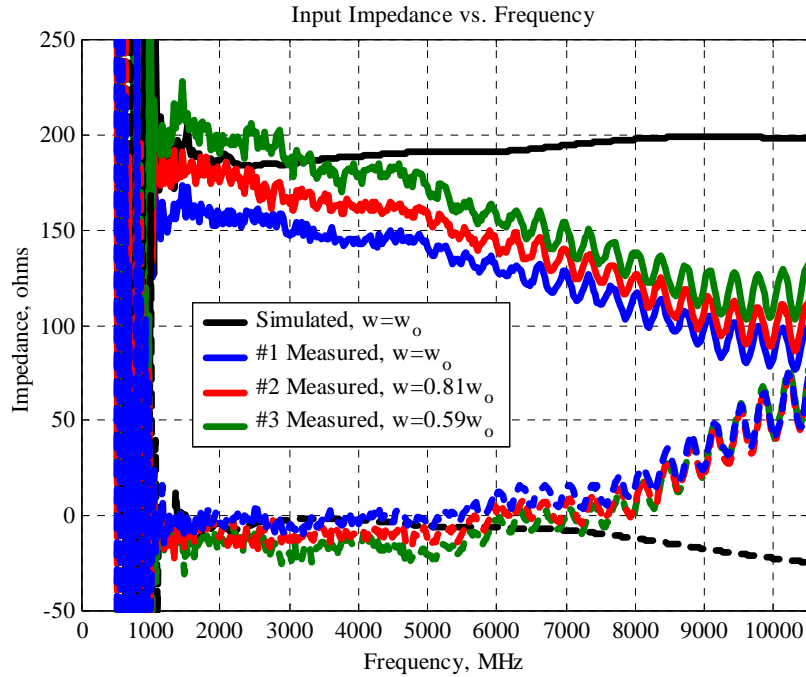


Figure 2.27 Comparison of measured input impedance versus frequency to simulated results for three different strip widths.

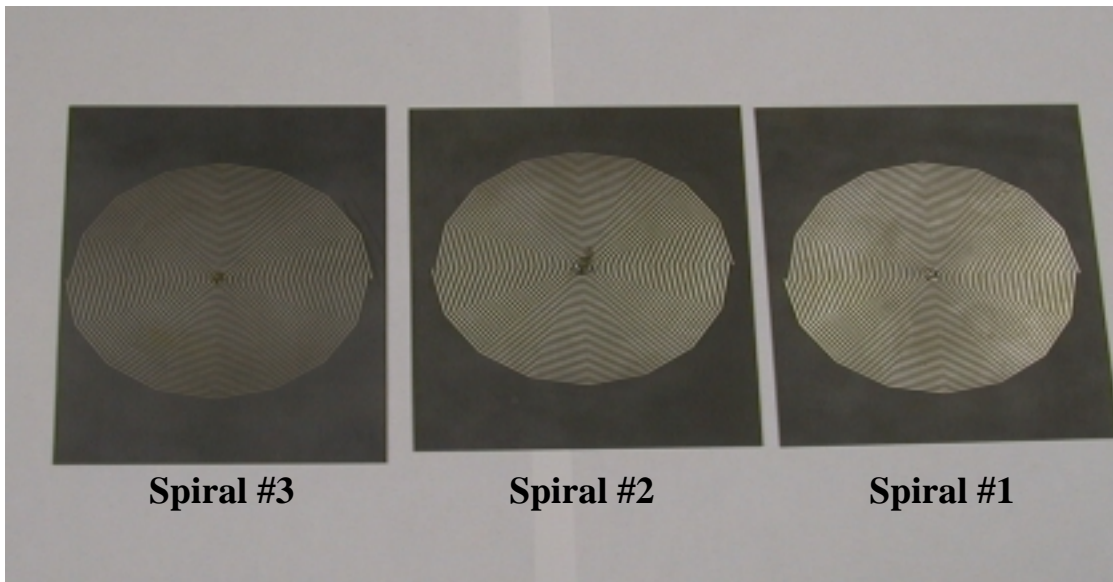


Figure 2.28 Measured spirals with different strip widths of Fig. 2.27.

The VSWR plot of Fig. 2.29 also shows the effect of the different strip widths. The simulated spiral is matched to 188 ohms and measured spirals are matched to 150 ohms, 165 ohms, and 185 ohms as strip width is reduced. The effect of adding loss to the

spiral is also demonstrated in Fig. 2.29. Using an ohmmeter, a loss of approximately 5 ohms/meter was measured along the length of each arm of the spiral. This effect is seen in the low frequency cutoff points for the spirals. All three of the measured spirals have a VSWR less than 2:1 at about 950 MHz while the simulated, lossless, spiral has a cutoff of about 1025 MHz. The theoretical low frequency cutoff of the spirals from (2.9) is 942 MHz, which is very close to the measured results. All of the spirals were measured using a 12 inch long feed made from 0.085 inch coax with k-connectors.

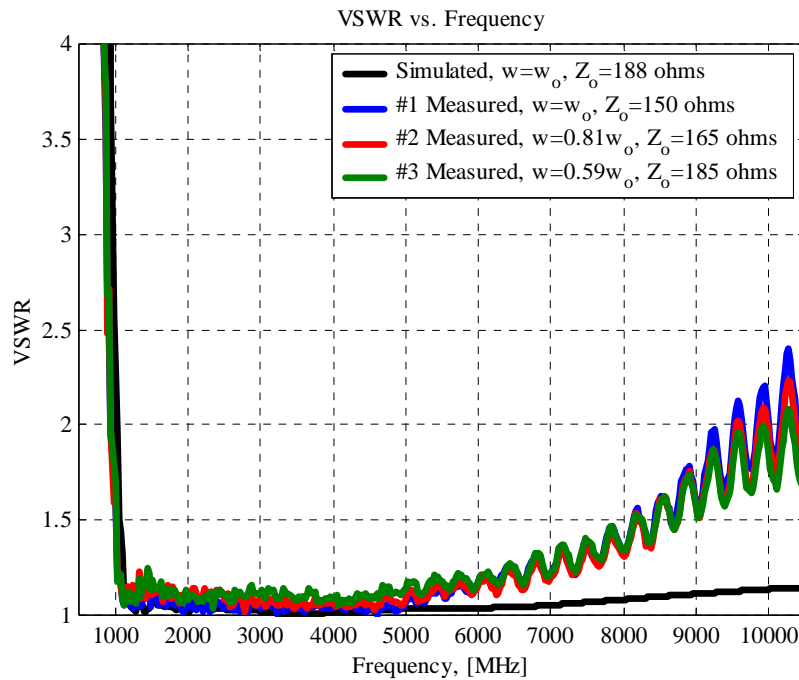


Figure 2.29 Comparison of measured VSWR versus frequency to simulated results for three different strip widths.

The patterns were measured using a wideband 180° hybrid and a feed made of 0.118" coax. The measurements were done at frequencies spanning from 900 MHz to 8000 MHz, which gives more than a 3-octave frequency sweep. A picture of the circular spiral that was used for pattern, gain, and axial ratio measurements is shown in Fig. 2.30. The hybrid insertion loss and impedance mismatch are plotted in Fig. 2.31. The impedance mismatch is referenced to 50 ohms since the standard gain horn used for gain measurements was matched to 50 ohms. The measured and simulated boresight gain of the circular spiral is shown in Fig. 2.32. Measured gain is shown with and without compensating for hybrid insertion loss and impedance mismatch loss. The measured gain

matches very well with the simulated gain for frequencies greater than 2000 MHz. Below 2000 MHz, the simulated gain is higher than the measured gain, but the trend of high, simulated gain at lower frequencies is common in the NEC4 results. The same effect was also seen in Figures 2.7 and 2.23. The measured boresight axial ratio is compared to simulated results in Fig. 2.33. The measured boresight axial ratio matches very well with the simulated results over the entire frequency range of interest. The radiation patterns and axial ratio patterns versus theta for the circular spiral are shown in Fig. 2.34 and Fig. 2.35, respectively. In general, the measured patterns match well with simulated results. Both the radiation patterns and axial ratio patterns become noisier with increasing frequency, which is due to current limitations of the measurement facility.

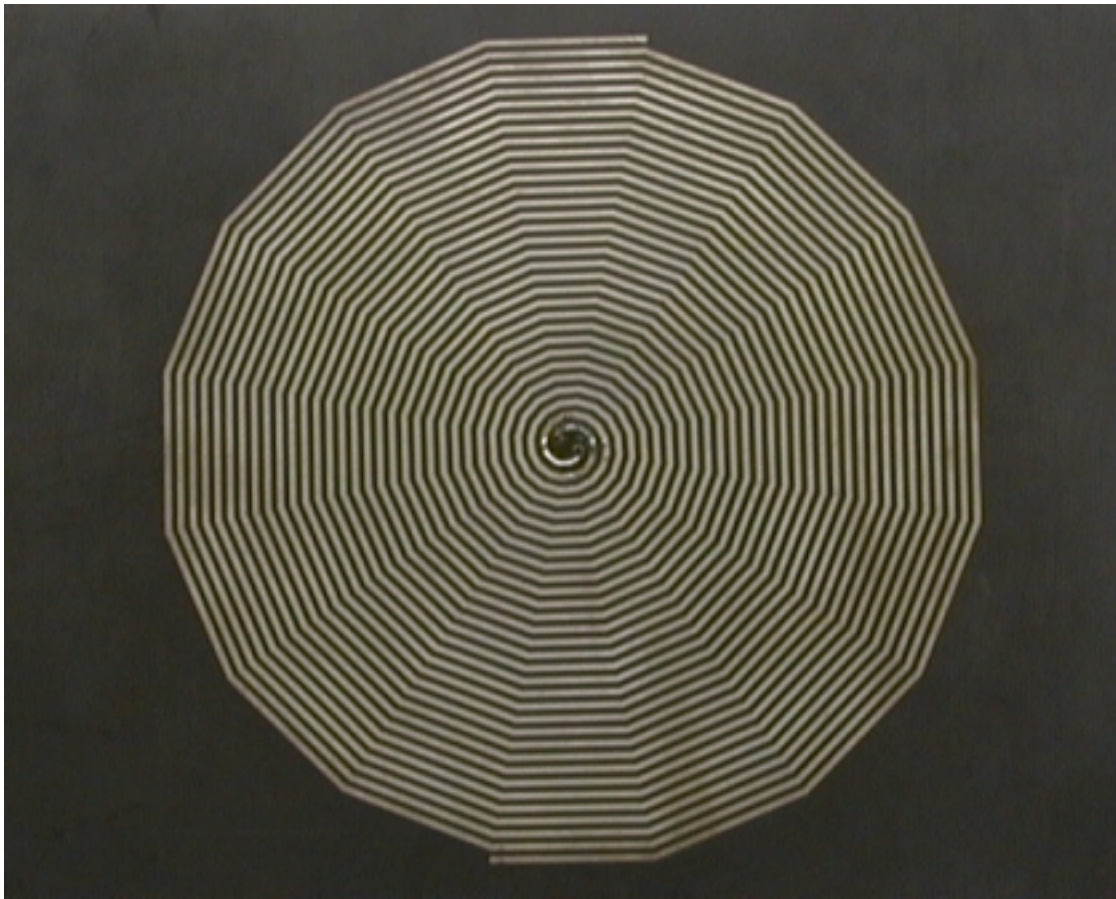


Figure 2.30 Circular spiral measured for pattern, gain, and axial ratio validation.

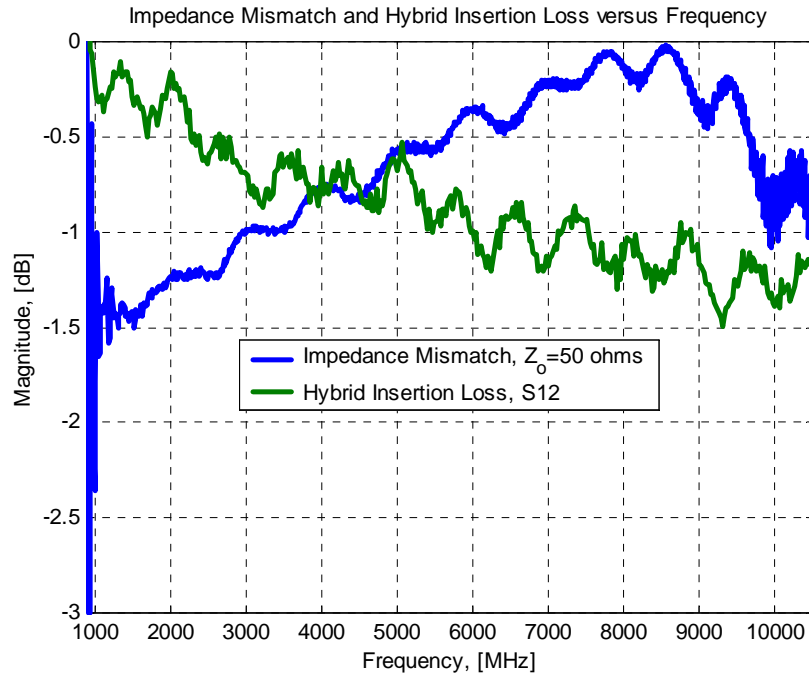


Figure 2.31 Measured hybrid insertion loss and impedance mismatch.

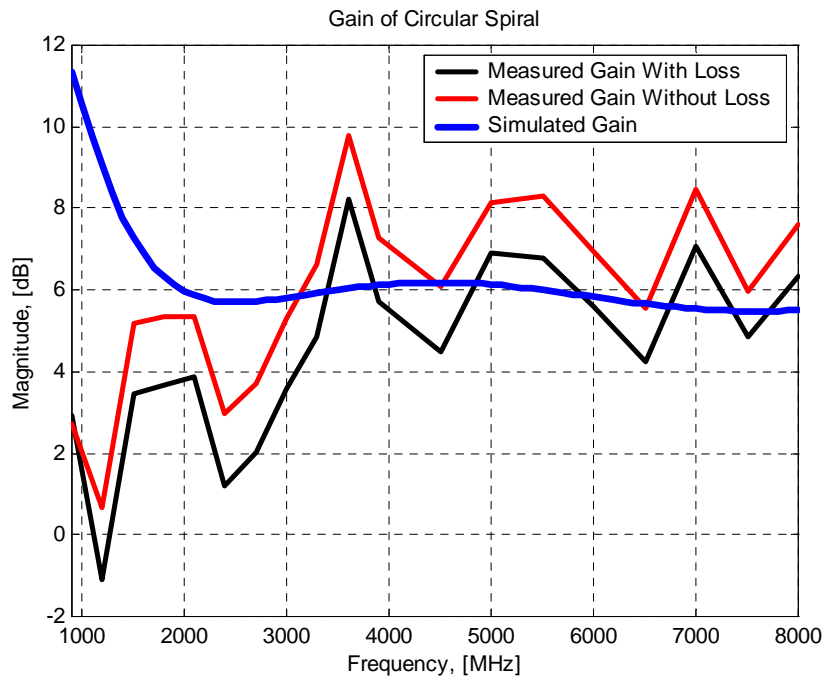


Figure 2.32 Measured hybrid insertion loss and impedance mismatch.

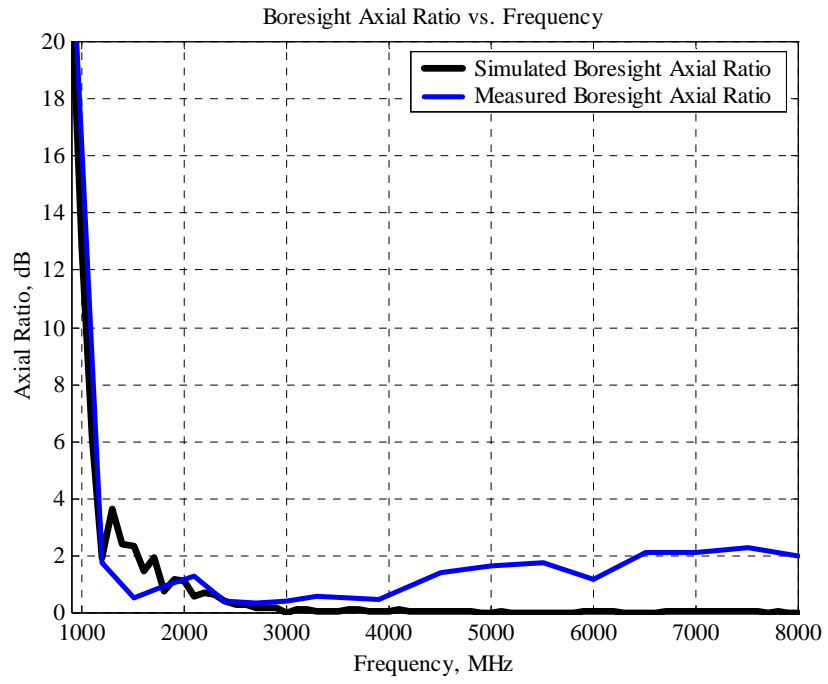


Figure 2.33 Comparison of measured and simulated axial ratio of circular spiral.

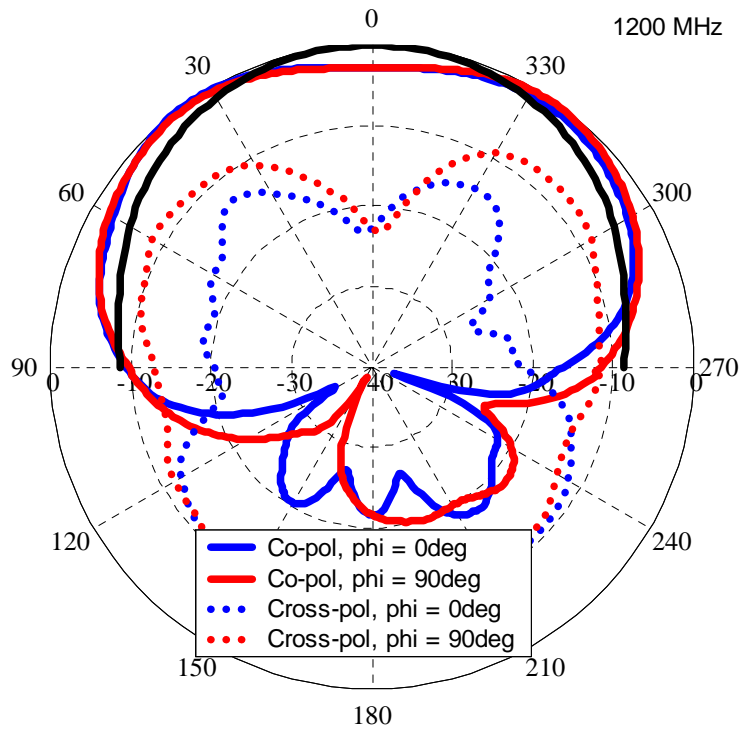
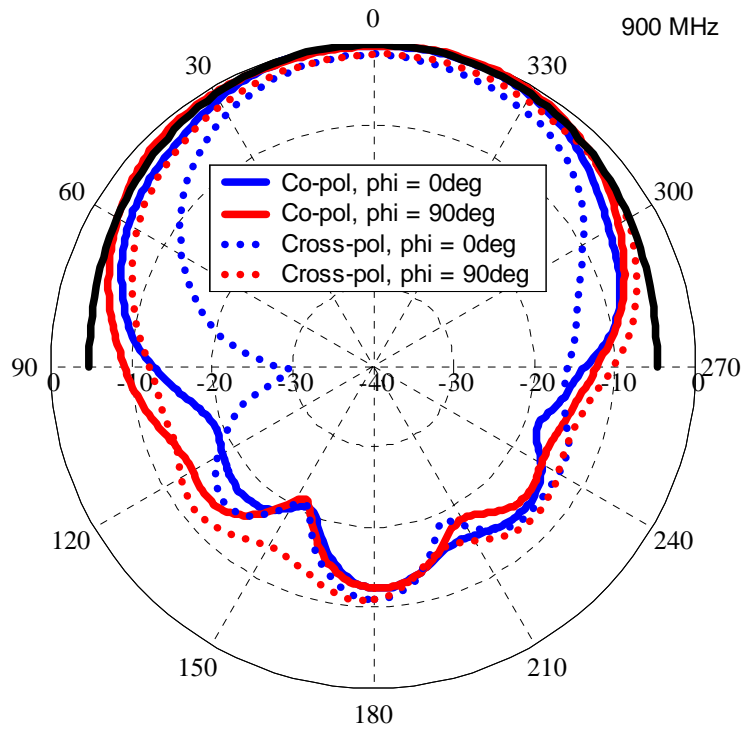


Figure 2.34 Measured radiation patterns of spiral in Fig 2.30. Theta cuts. Black line is simulated result.

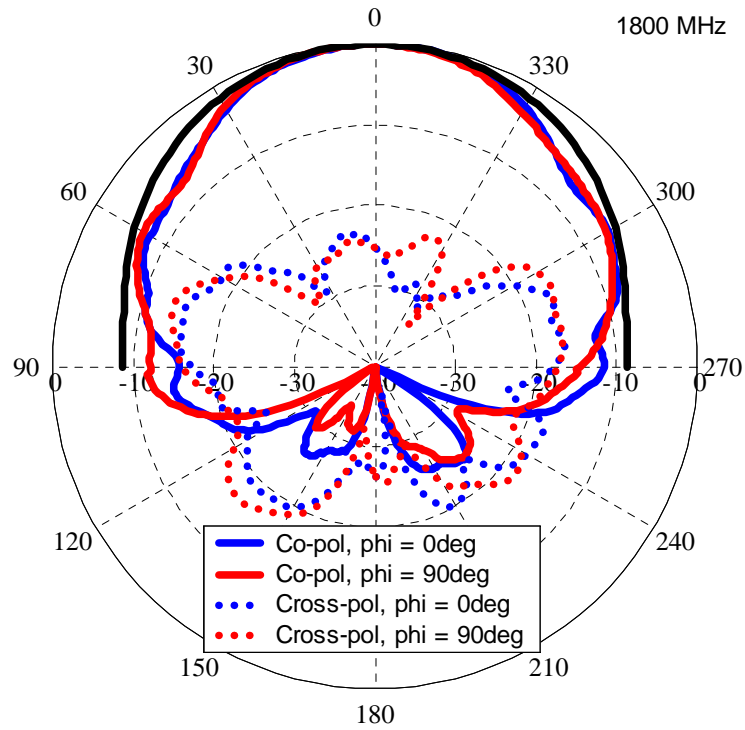
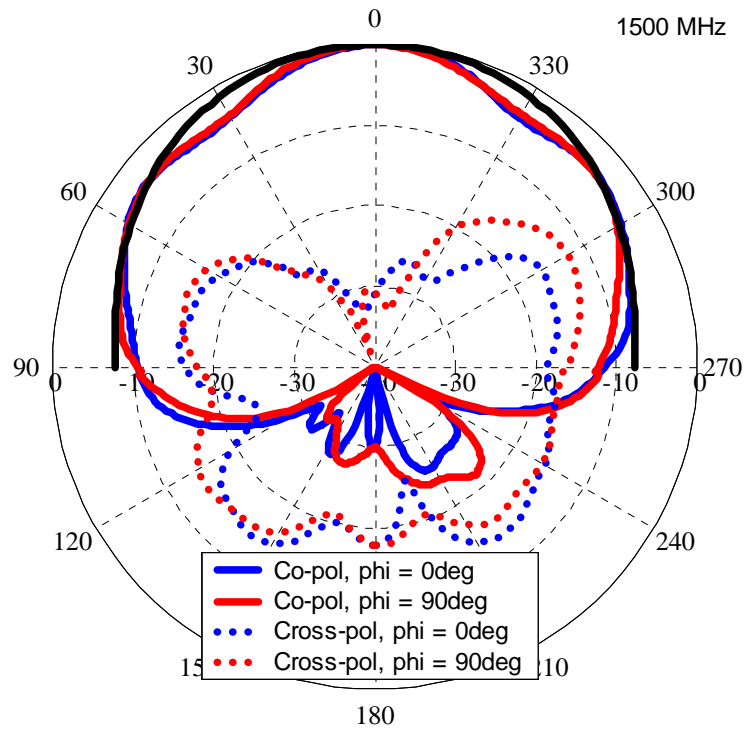


Figure 2.34 (cont) Measured radiation patterns of spiral in Fig 2.30. Theta cuts. Black line is simulated result.

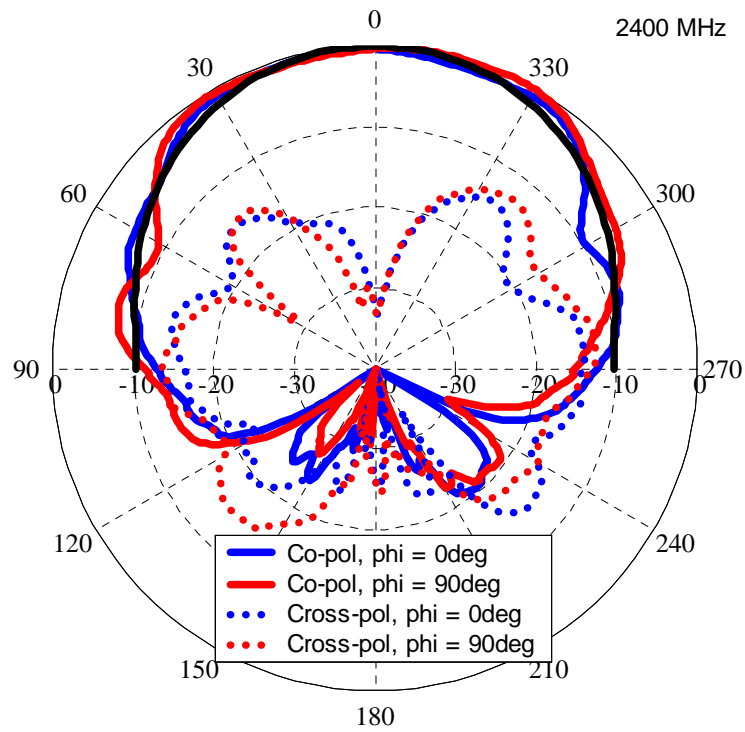
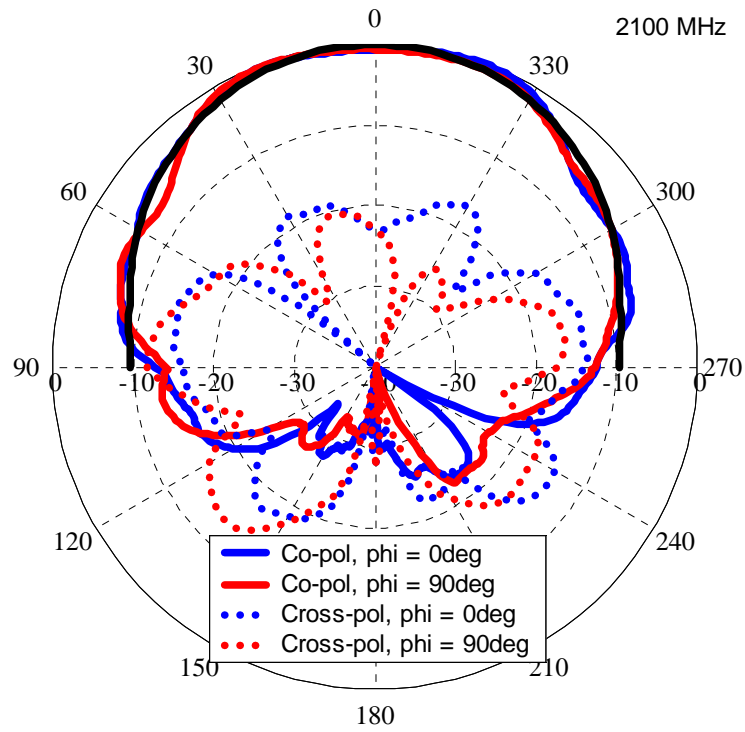


Figure 2.34 (cont) Measured radiation patterns of spiral in Fig 2.30. Theta cuts. Black line is simulated result.

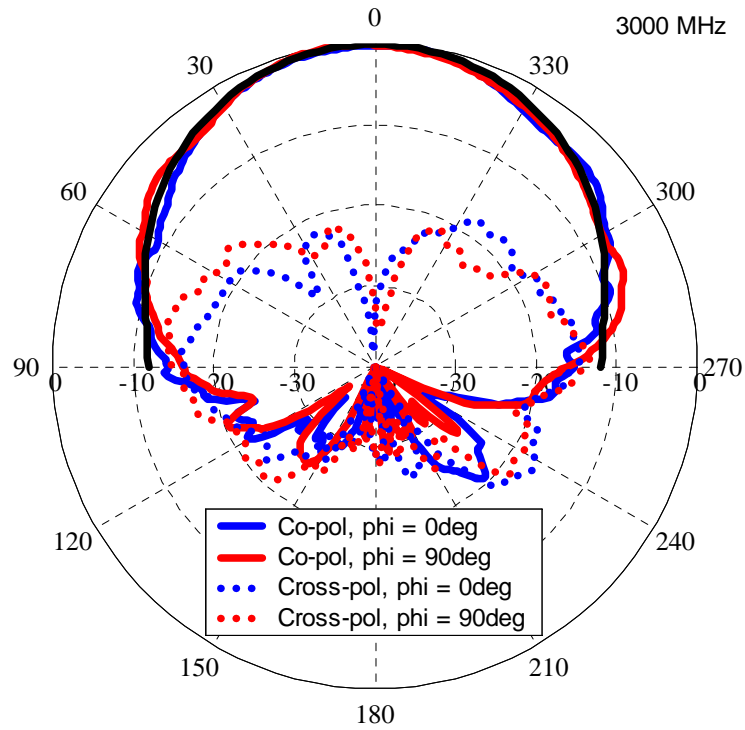
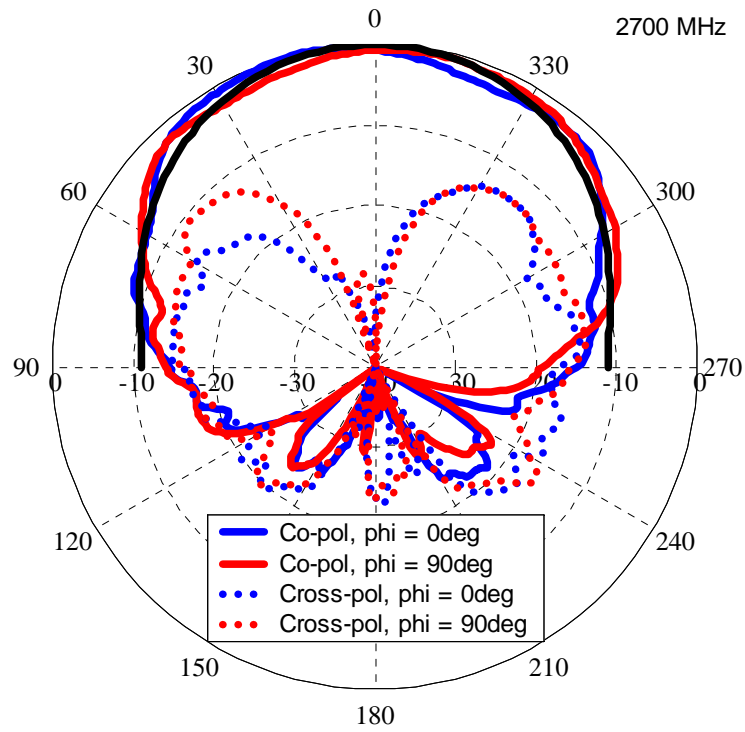


Figure 2.34 (cont) Measured radiation patterns of spiral in Fig 2.30. Theta cuts. Black line is simulated result.

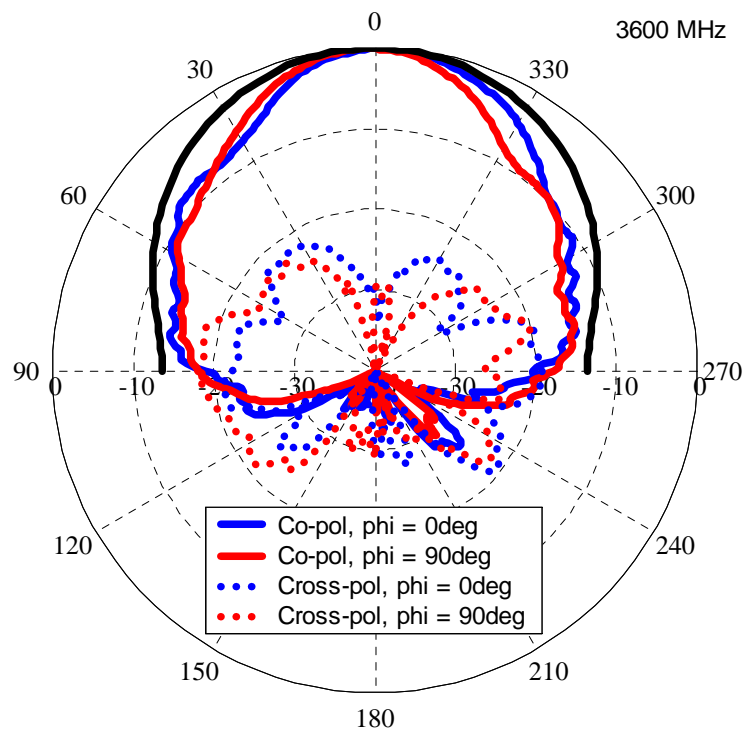
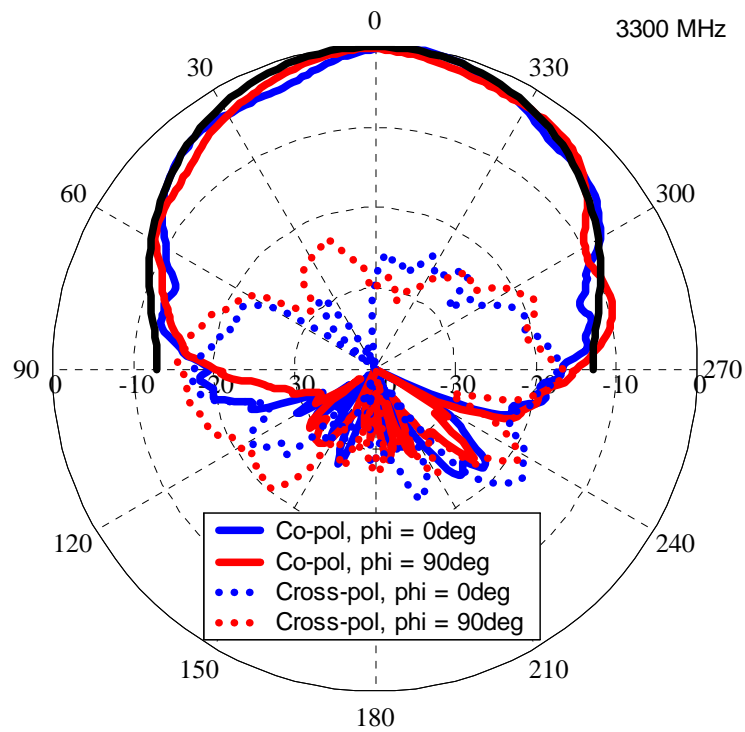


Figure 2.34 (cont) Measured radiation patterns of spiral in Fig 2.30. Theta cuts. Black line is simulated result.

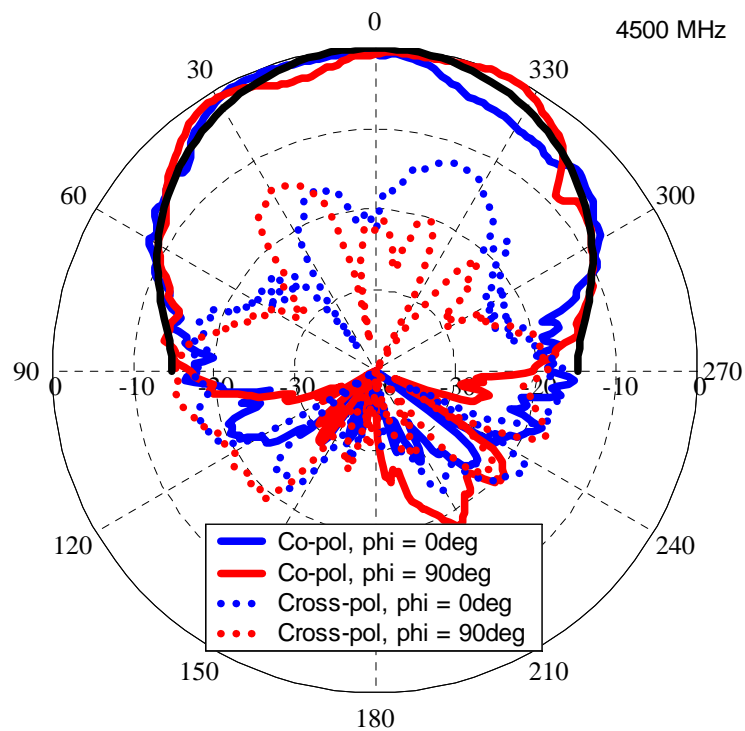
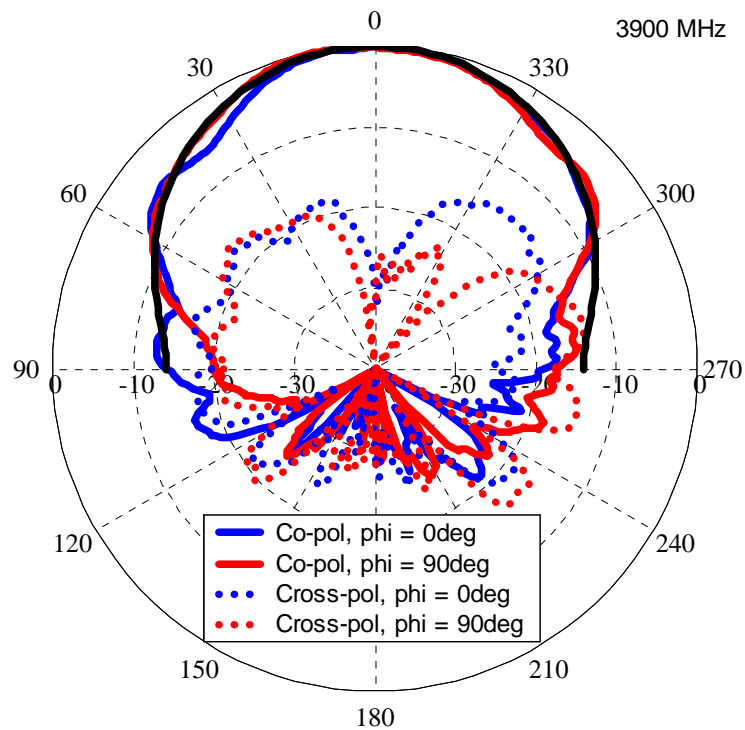


Figure 2.34 (cont) Measured radiation patterns of spiral in Fig 2.30. Theta cuts. Black line is simulated result.

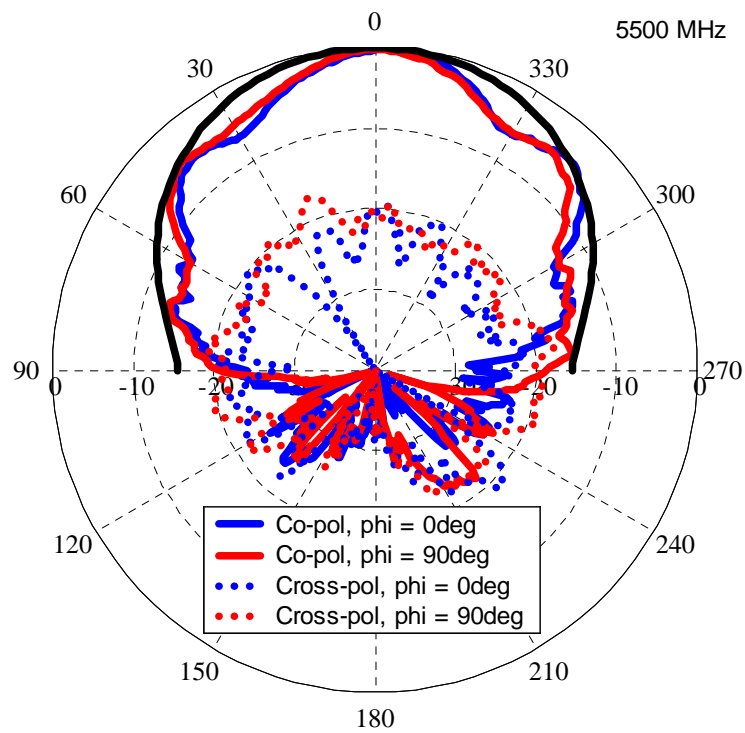
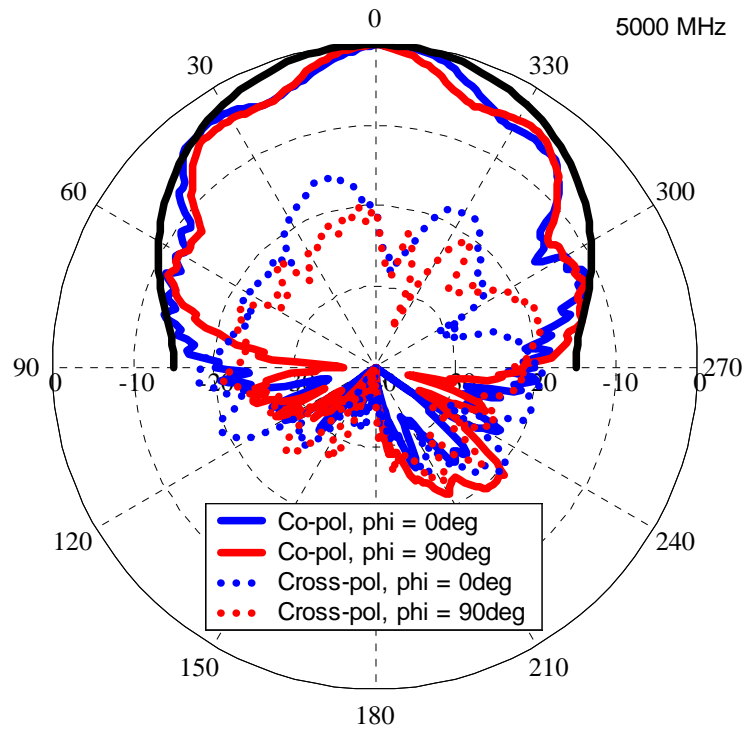


Figure 2.34 (cont) Measured radiation patterns of spiral in Fig 2.30. Theta cuts. Black line is simulated result.

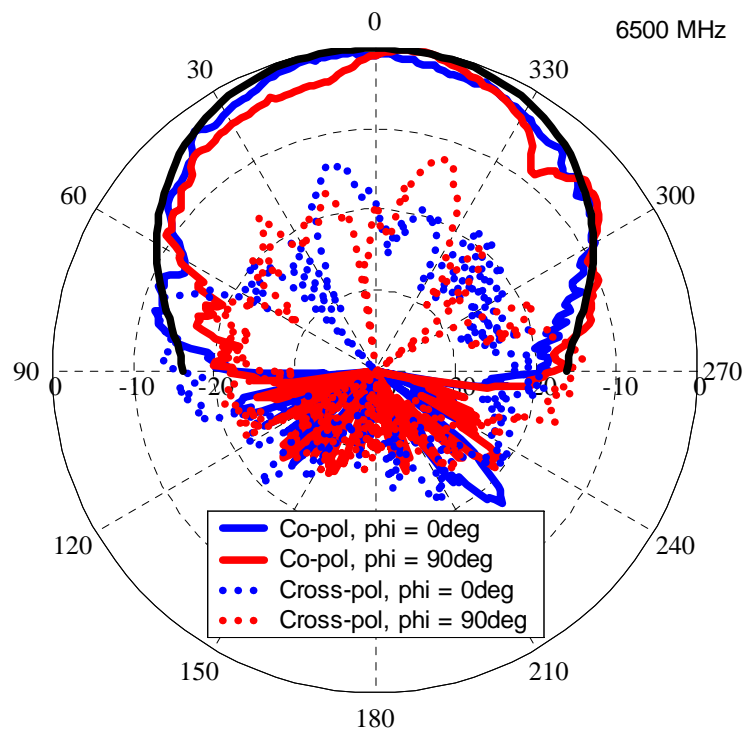
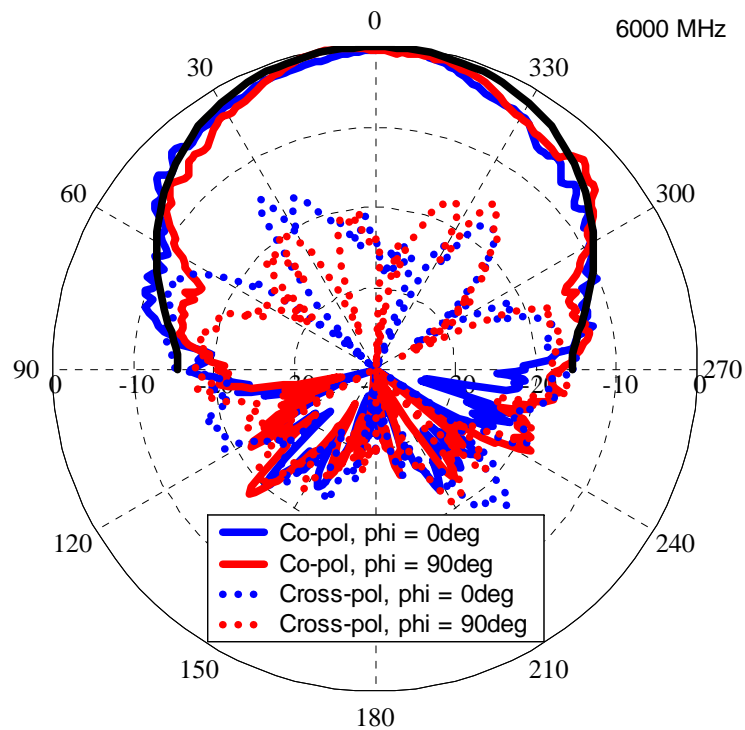


Figure 2.34 (cont) Measured radiation patterns of spiral in Fig 2.30. Theta cuts. Black line is simulated result.

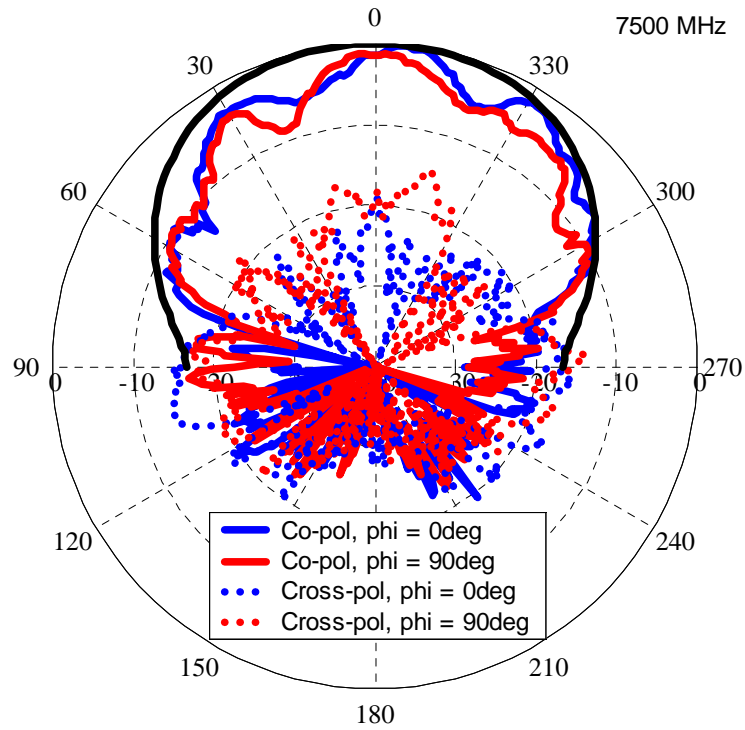
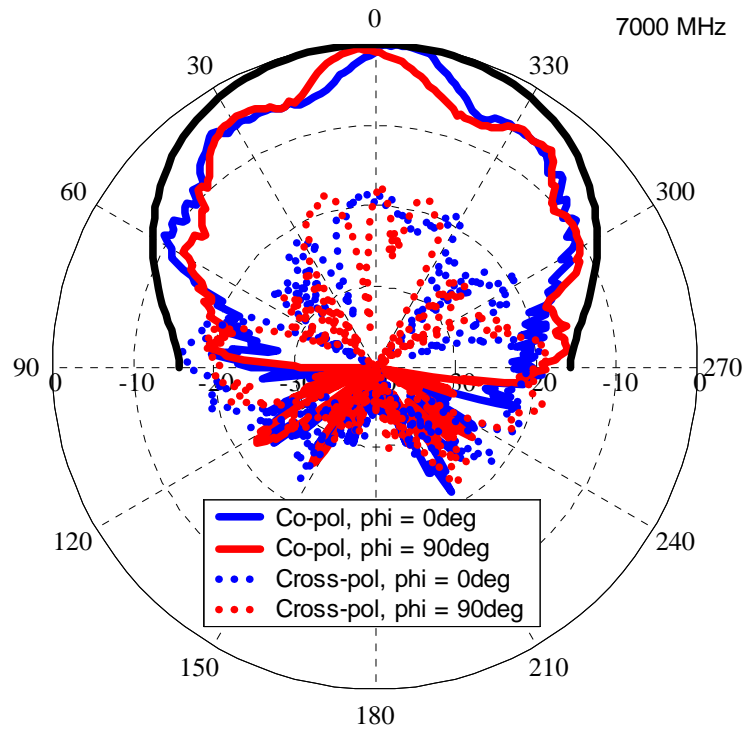


Figure 2.34 (cont) Measured radiation patterns of spiral in Fig 2.30. Theta cuts. Black line is simulated result.

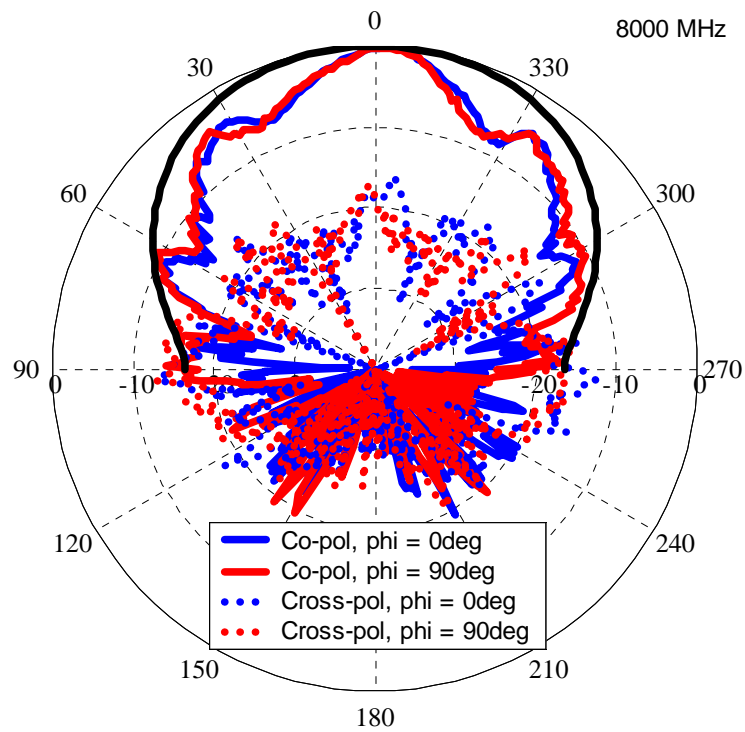


Figure 2.34 (cont) Measured radiation patterns of spiral in Fig 2.30. Theta cuts. Black line is simulated result.

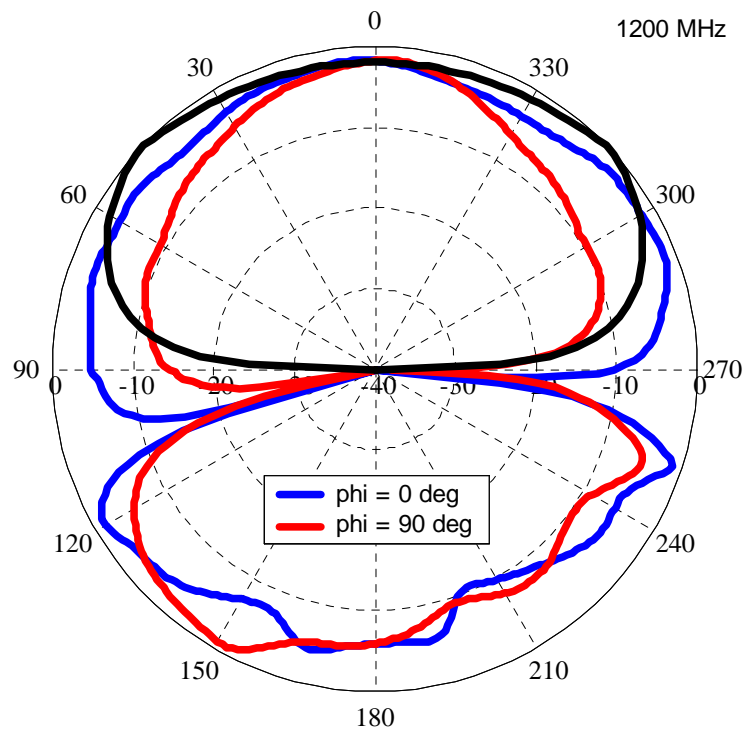
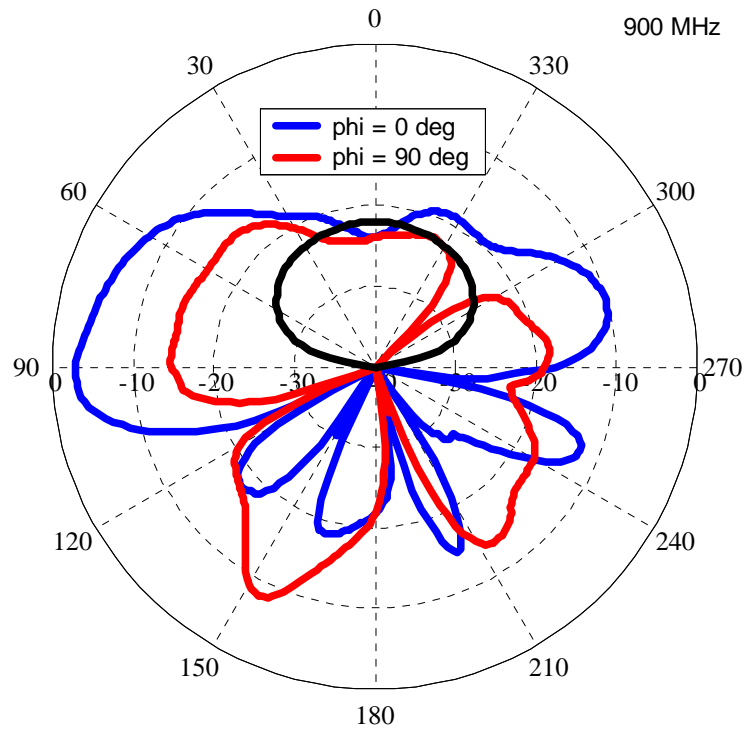


Figure 2.35 Measured axial ratio of spiral in Fig 2.30. Theta cuts. Black line is simulated result.

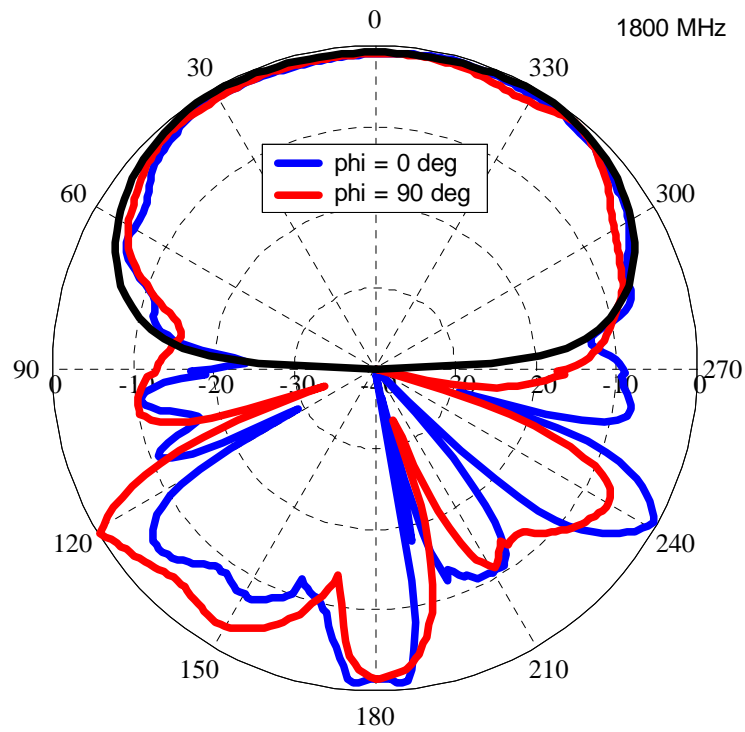
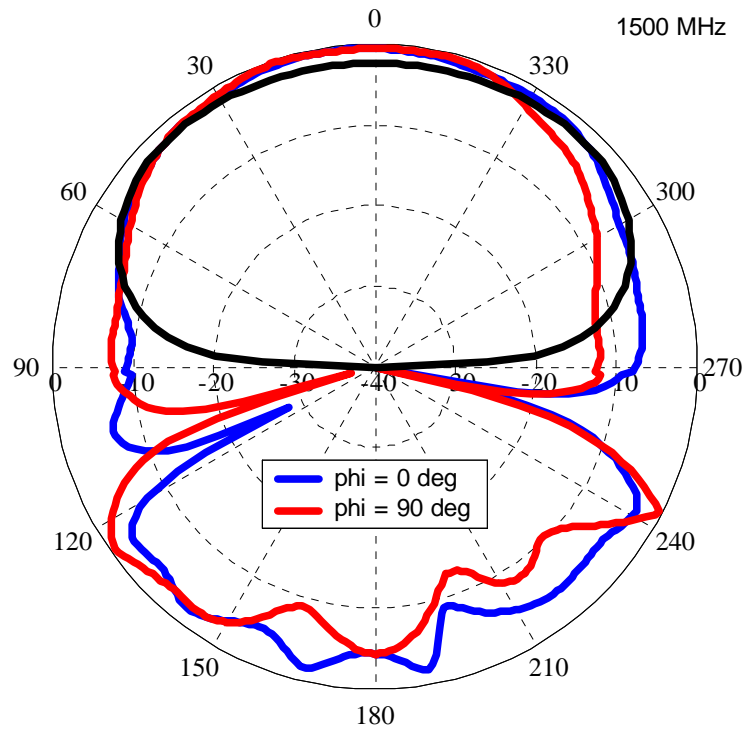


Figure 2.35 (cont) Measured axial ratio of spiral in Fig 2.30. Theta cuts. Black line is simulated result.

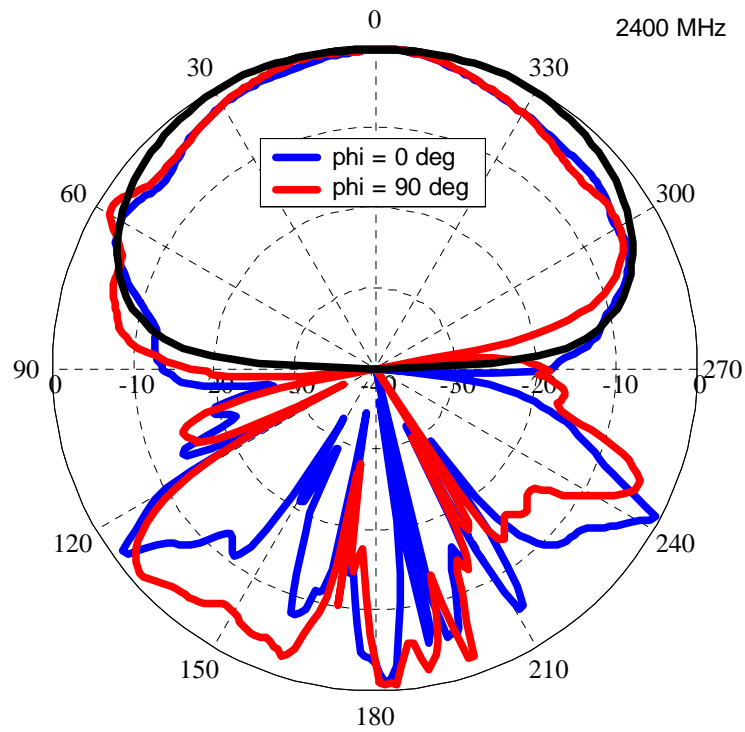
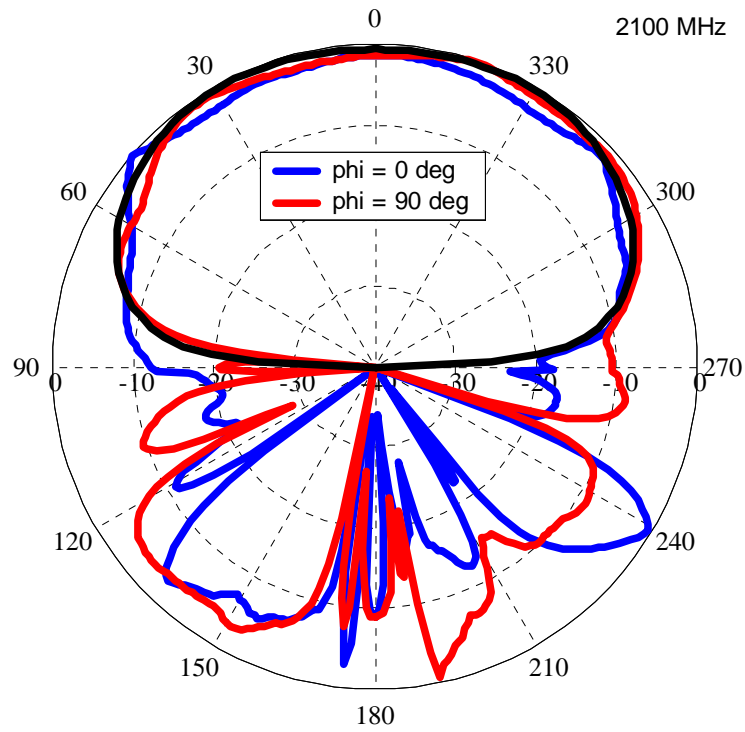


Figure 2.35 (cont) Measured axial ratio of spiral in Fig 2.30. Theta cuts. Black line is simulated result.

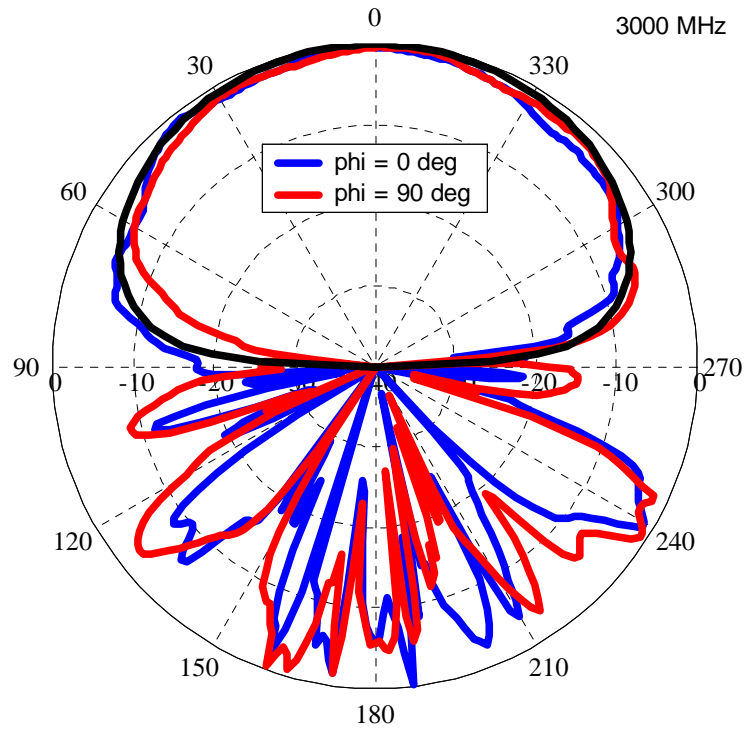
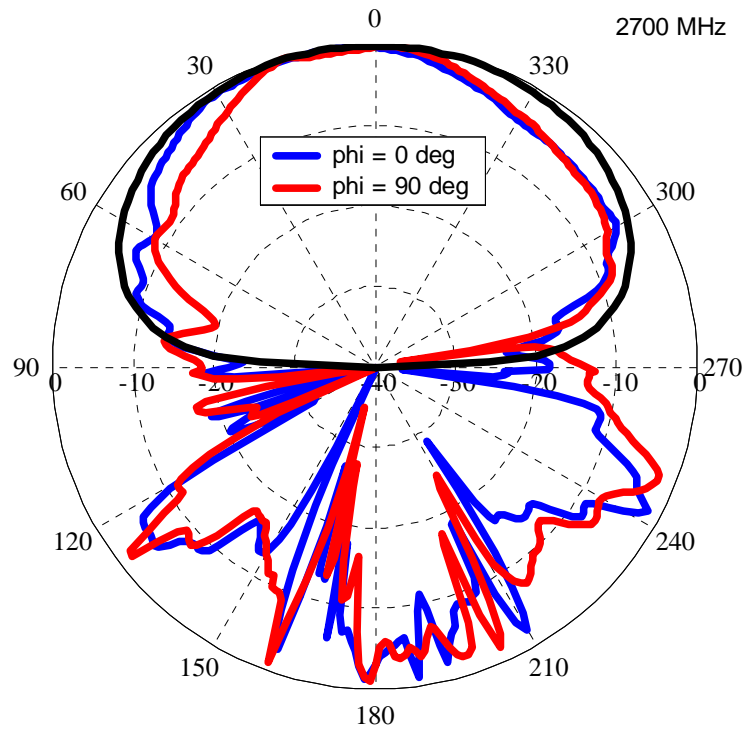


Figure 2.35 (cont) Measured axial ratio of spiral in Fig 2.30. Theta cuts. Black line is simulated result.

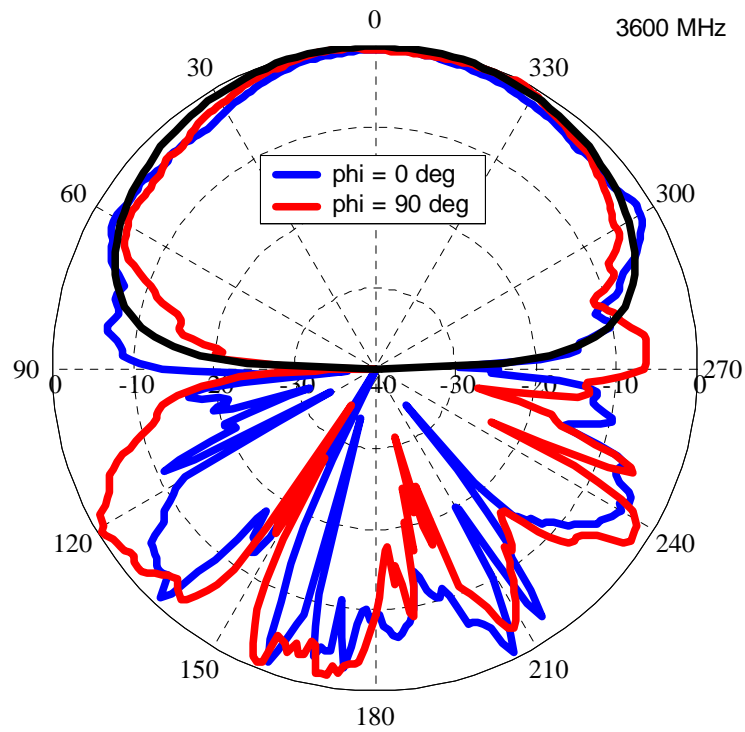
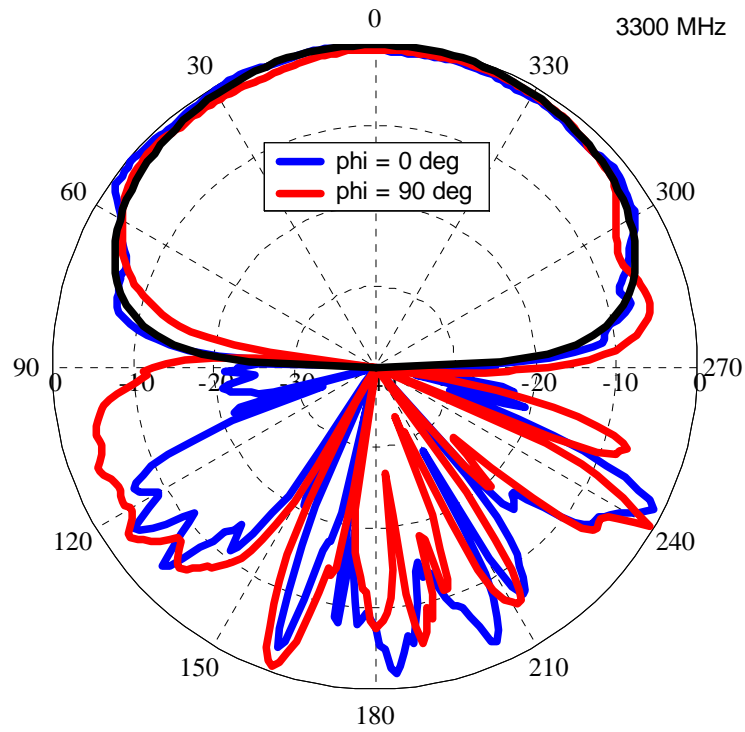


Figure 2.35 (cont) Measured axial ratio of spiral in Fig 2.30. Theta cuts. Black line is simulated result.

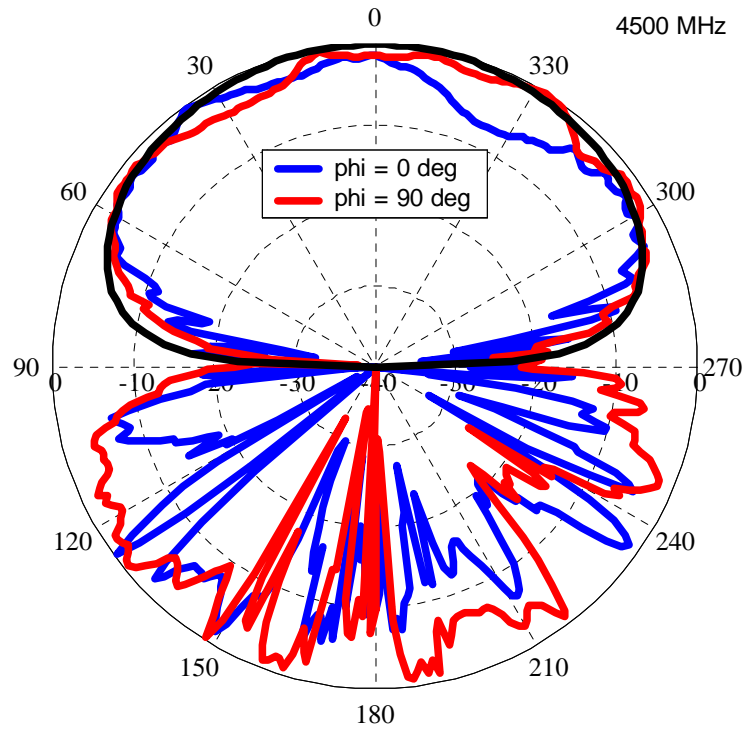
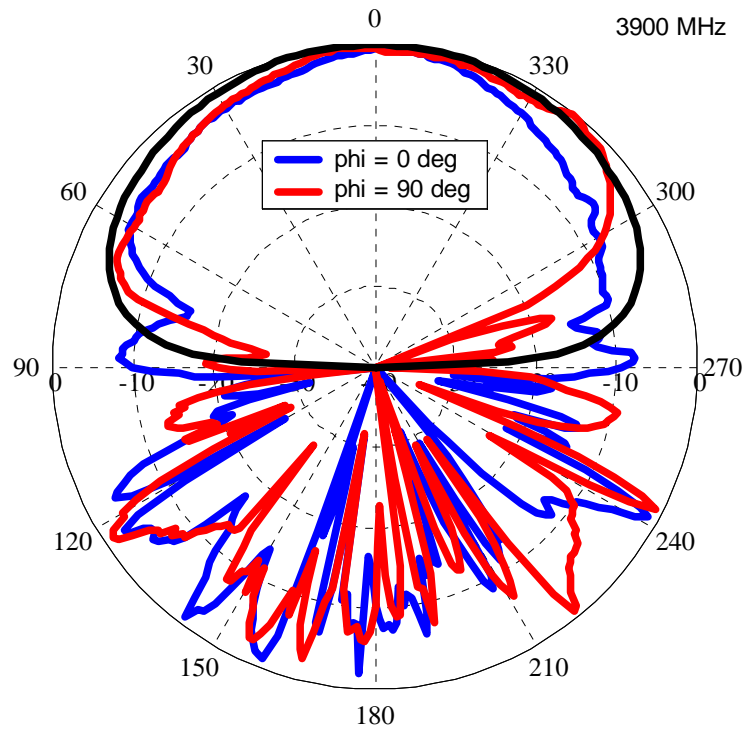


Figure 2.35 (cont) Measured axial ratio of spiral in Fig 2.30. Theta cuts. Black line is simulated result.

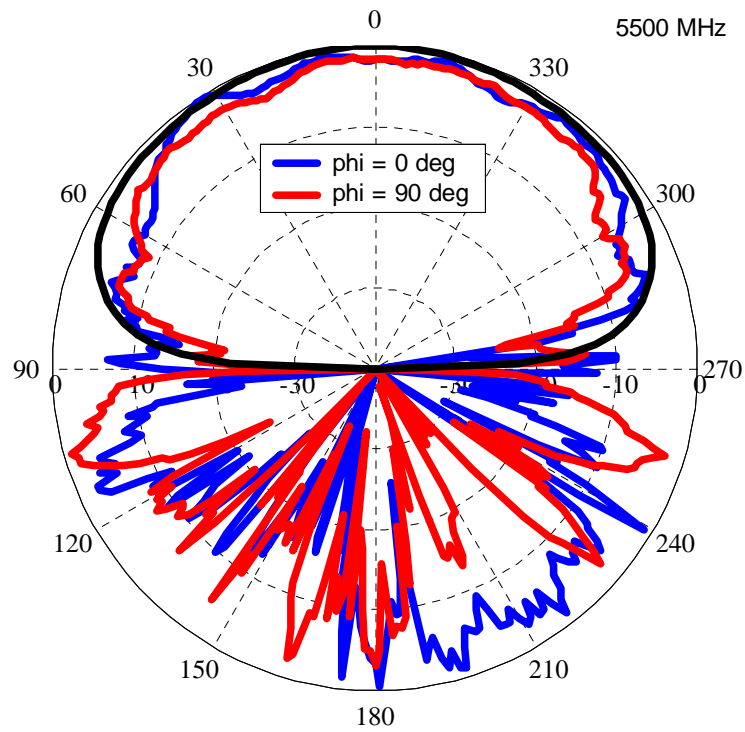
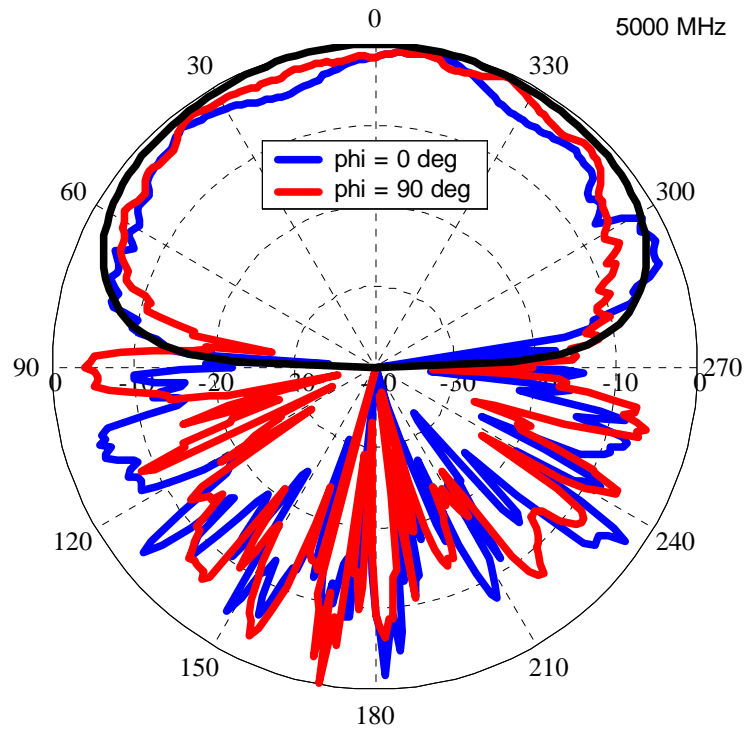


Figure 2.35 (cont) Measured axial ratio of spiral in Fig 2.30. Theta cuts. Black line is simulated result.

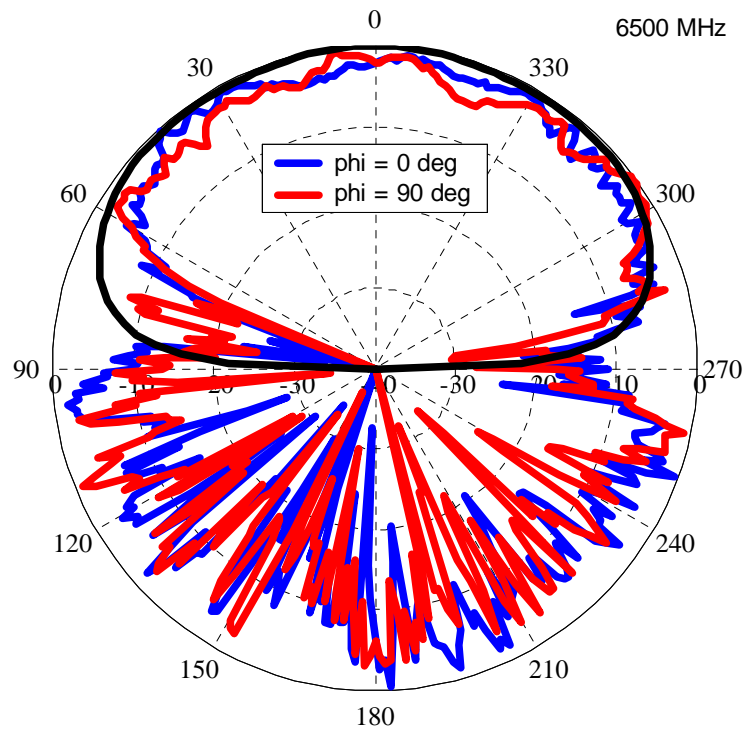
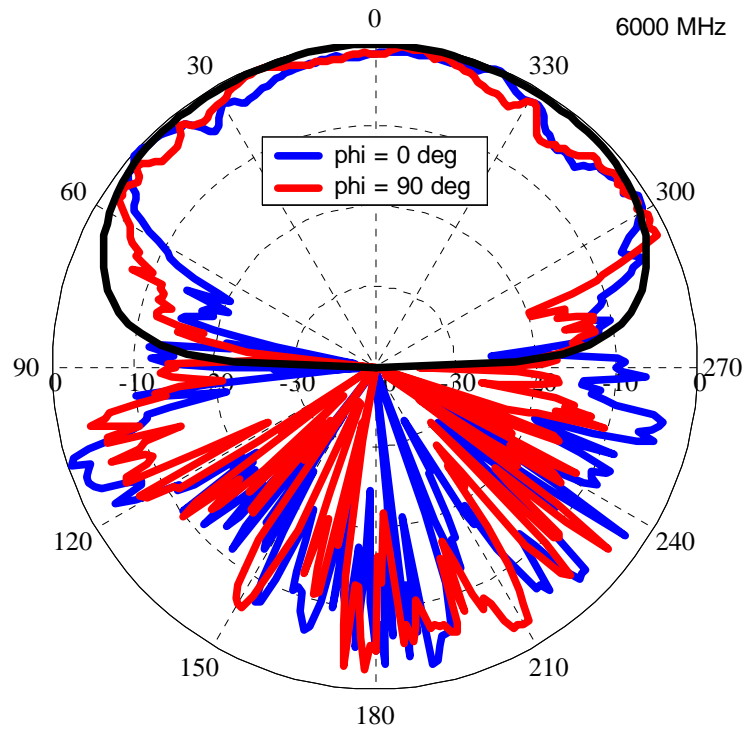


Figure 2.35 (cont) Measured axial ratio of spiral in Fig 2.30. Theta cuts. Black line is simulated result.

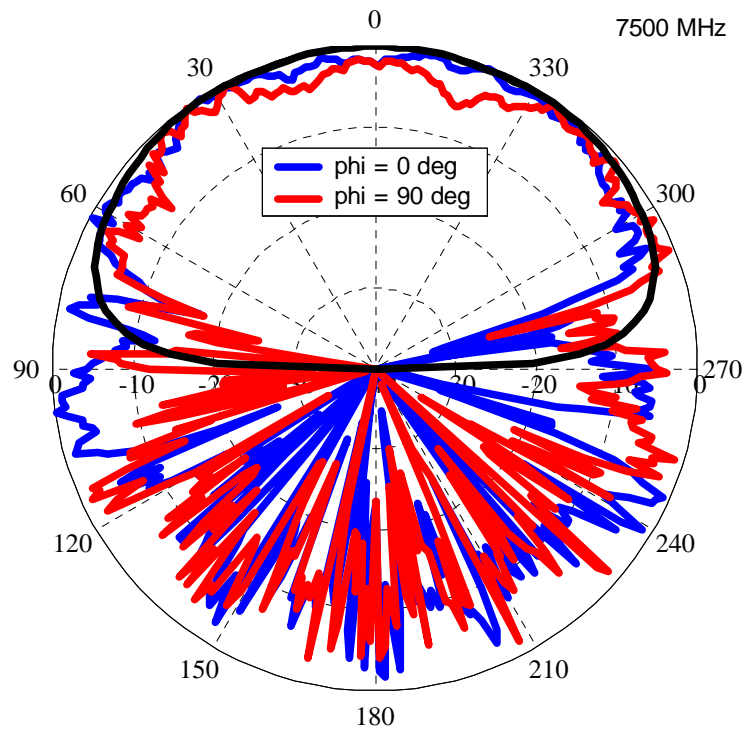
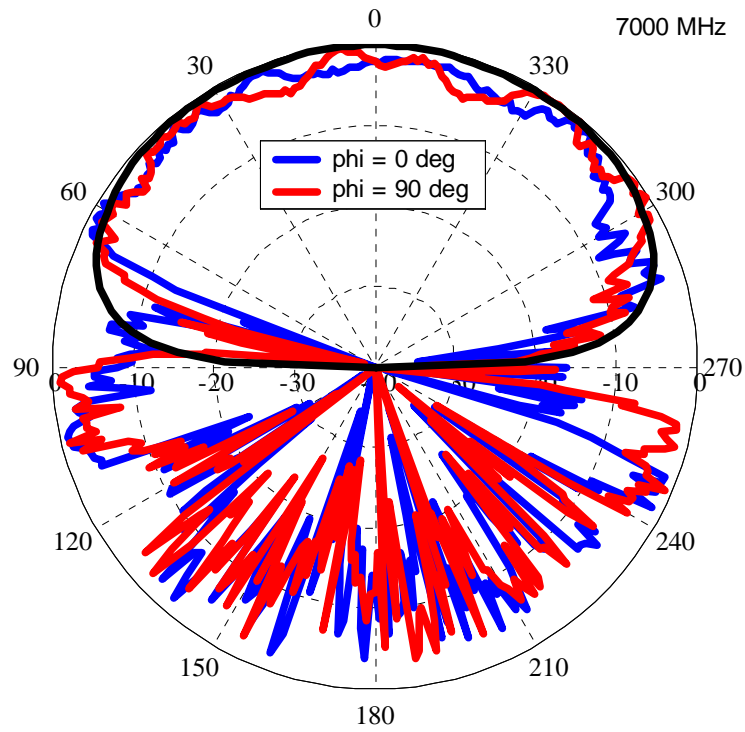


Figure 2.35 (cont) Measured axial ratio of spiral in Fig 2.30. Theta cuts. Black line is simulated result.

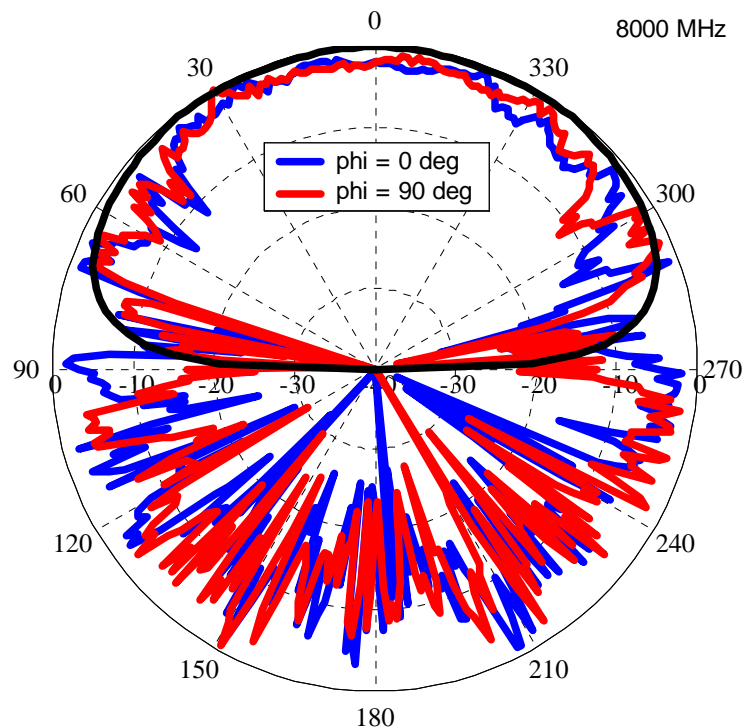


Figure 2.35 (cont) Measured axial ratio of spiral in Fig 2.30. Theta cuts. Black line is simulated result.

2.6 Summary

The basic theory and the necessary information to correctly simulate an Archimedean spiral antenna in NEC4 have been presented in this chapter. The Archimedean spiral is a complementary antenna structure having a theoretical input impedance of 188 ohms. For satisfactory simulation results in NEC4, the inner radius of the spiral should equal the width of each arm and a wire with a radius of one quarter the wire width should be used to model each arm. It was also found that using 16 segments per turn and 5 segments on the feed wire yielded adequate simulation results. Spiral performance can be improved by adding conductivity loss or resistive loading to the end of each arm to reduce reflections from the end of the spiral and improve low frequency impedance performance. Also, the spiral can be used over a ground plane for a wide frequency range by using a lossy ground plane or by using a conical ground plane to prevent pattern nulls. Input impedance, pattern, and axial ratio of a circular spiral printed on RT/Duroid 5880 were measured. The measurements matched very well with

simulated results and help to validate the NEC4 simulations used throughout this dissertation.